Front. Energy 2025, 19(4): 450–470
https://doi.org/10.1007/s11708-025-0996-2

REVIEW ARTICLE

Recent advancements in all-inorganic and organic-inorganic hybrid metal halide materials for photocatalytic CO_2 reduction reaction

Ruhao Chen[1#], Cunbi Wang[1#], Xu Zhang[2], Chengdong Peng (✉)[1], Chao Lin[1], Gaokun Chen[1], Yuexiao Pan (✉)[1]

1 Key Laboratory of Carbon Materials of Zhejiang Province, College of Chemistry and Materials Engineering, Wenzhou University, Wenzhou 325035, China
2 Faculty of Science, Department of Chemistry, National University of Singapore, Singapore 119077, Singapore

Abstract The utilization of solar energy to address energy and environmental challenges has a seen a significant growth in recent years. Metal halides, which offer unique advantages such as tunable bandgaps, high light absorption efficiencies, favorable product release rates, and low exciton binding energies, have emerged as excellent photocatalysts for energy conversion. This paper reviews the recent advancements in both all-inorganic and organic-inorganic hybrid metal halide photocatalytic materials, including the fundamental mechanisms of photocatalytic CO_2 reduction, various synthesis strategies for metal halide photocatalysts, and their applications in the field of photocatalysis. Finally, it examines the current challenges associated with metal halide materials and explores potential solutions for metal halide materials, along with their future prospects in photocatalysis applications.

Keywords metal halide, photocatalysts, organic-inorganic hybrid, all-inorganic, photocatalytic CO_2 reduction

1 Introduction

In today's world, rapid development of industry and growing global population [1–3] have led to increased exploitation and excessive consumption of fossil fuels [4], resulting in an energy shortage crisis and worrying global environmental situation [5]. The issue of the greenhouse effect, particularly the excessive emission of carbon dioxide (CO_2) and its slow conversion, is gaining increasing attention from the scientific community. This poses a significant threat to ecosystems, making it urgent to address and resolve this problem [6]. It is imperative to develop sustainable and environmentally friendly technologies [7–9], to achieve the goals of Sustainable Development Strategy, such as "carbon peak" and "carbon neutrality" in the future [10].

Fortunately, inspired by the photosynthetic behavior of plants, it is undoubtedly a wise choice to transform CO_2 into valuable materials such as methane, ethanol, or other usable green fuels using solar energy under certain reactions [11–16]. Solar energy, being clean, stable, and renewable, serves a reliable source of energy for humanity [17,18]. However, due to the intermittent of sunlight, solar energy cannot be directly used as an energy source for daily life. Therefore, in recent years, the conversion of solar energy has gradually attracted extensive attention from all walks of life [19,20]. Artificial photosynthesis, also known as photocatalysis, has been developed as an effective strategy to convert solar energy into clean energy [21,22], which not only helps alleviate the energy crisis, but also mitigates the excessive emission of greenhouse gases [23–26].

Generally, the photocatalytic CO_2 reduction reaction (CO_2RR) involves three processes: photoabsorption and generation of photogenerated charge carriers, separation and transfer of photogenerated carriers, and reduction of CO_2 into other substances by active sites on the photocatalyst surface [27–29].

Received Dec. 6, 2024; accepted Feb. 17, 2025; online Mar. 25, 2025
Correspondences: Chengdong Peng, cdpeng@wzu.edu.cn;
Yuexiao Pan, yxpan@wzu.edu.cn

[#] The two authors contributed equally to this work.

For an ideal photocatalyst to achieve higher efficiency in solar-energy conversion, the following features are essential: strong absorption of visible light, high carrier separation efficiency with a low recombination rate of photoelectron-hole pairs, and higher CO_2 reduction activity at the surface [30].

Semiconductor materials, with their effective light absorption and ingenious bandgaps, can meet these requirements by generating electron-hole pairs crucial for surface-initiated photocatalytic reactions [22,29,31]. Both all-inorganic and organic-inorganic hybrid semiconductor photocatalysts have garnered significant attention due to their excellent utilization of light and customizable structures. Among these, metal halides have emerged as one of the optimal options due to their unique properties, including strong absorption capability of visible light, tunable structures, negative conduction band positions, exceptional capability of charge transport, ease of synthesis, low fabrication costs, favorable for large-scale production, and low exciton binding energies. In fact, metal halide-based materials do have ideal development potential in this field and have been successfully developed as efficient photocatalysts [32–37].

However, such materials inevitably do present certain challenges. The separation and transport of photogenerated charges are severely hindered by significant energy defects, limiting their practical applications in terms of photocatalytic activity and cycling stability. In addition, the toxicity of lead in some of the best performing lead halide materials prevent their mass production. Apparently, there are many challenges in the current photocatalysis of CO_2, and corresponding solutions are urgently needed, which means that further improvement of photocatalysts is of great practical significance [38–40].

This review summarizes the latest progress in the use of perovskite and non-perovskite metal halides for photocatalytic CO_2RR from both organic-inorganic hybrids and all-inorganic perspectives. It begins with an introduction to the mechanism of photocatalytic CO_2 reduction, followed by an overview of common synthesis methods, including hydrothermal and anti-solvent precipitation. Afterwards, it provides a more detailed discussion on typical metal halide photocatalysts and relevant improvement strategies. Finally, it discusses future research challenges for metal halide photocatalysts, and offers positive and optimistic insights into their potential development prospects, especially in terms of improving stability, environmental friendliness, and product value. It is hoped that this review will provide a unique perspective on the development of metal halide photocatalysts and inspire innovative research in the fields of energy and material science.

2 Basic mechanism of photocatalytic CO_2 reduction

The process of photocatalytic CO_2RR begins when CO_2 molecules are adsorbed onto the catalyst surface, shown in Fig. 1. Upon absorbing solar energy, photocatalysts generate photoexcited electron-hole pairs. This portion of energy must be at least equal to or greater than the bandgap value of the semiconductor (usually represented as E_g). Then, the excited photoelectrons migrate to the conduction band (CB), while the holes remain trapped in the valence band (VB). Further, these photogenerated electrons and holes move to the semiconductor surface, where the CO_2 molecules are adsorbed. Finally, CO_2RR occurs at catalytic active sites, where electrons are utilized. Concurrently, oxidation reactions mediated by holes are also stimulated, such as the decomposition of water to produce oxygen.

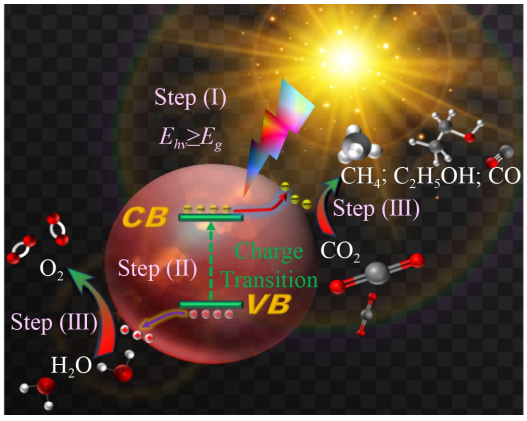

Fig. 1 Photocatalytic CO_2 reduction process, including light absorption, electronic transitions, and formation of target products.

In general, both all-inorganic or organic-inorganic hybrid metal halide materials follow a similar mechanism in photocatalytic reduction of CO_2. However, there are distinct differences between the two. On the one hand, the orderly arrangement of organic components in hybrid materials may form efficient carrier transport channels, thereby enhancing carrier separation efficiency [41]. On the other hand, fully inorganic metal halide materials, such as $CsPbBr_3$, primarily activate CO_2 molecules through coordination with metal ions during the photoreduction process of CO_2. The reaction pathway is relatively straightforward, and the products are usually dominated by simple hydrocarbons like CO [42]. Organic cation engineering is expected to optimize the band edge and overall photocatalytic performance for CO_2 reduction of these materials. Some reported modifications, such as alkylation, can significantly increase the maximum occupied molecular orbital energy of cations, leading to increased product diversity [43].

Based on the above mechanism, it is clear that the catalytic efficiency of CO_2 reduction is determined by the adsorption of CO_2 molecules onto the catalyst surface. A high specific surface area (BET) is a primary requirement for effective catalysis. As is well known, CO_2 is an exceptionally self-stable molecule, with the decomposition of its carbon-oxygen double bond requiring 750 kJ/mol, or even as high as 803 kJ/mol. Hence, in the catalytic reduction of CO_2, energy higher than the activation energy barrier is needed to drive the reaction forward [30]. Furthermore, from the perspective of electrode potential, as shown in Table 1 below, the redox potential for the conversion of CO_2 molecules into reaction intermediate $*CO_2^-$ is approximately −1.90 eV, using a normal hydrogen electrode (NHE) as a reference. Therefore, it is extremely difficult to achieve the generation of $*CO_2^-$ solely by transferring a single electron.

Table 1 Possible electrochemical reduction reaction pathways of CO_2 and their corresponding electrode potentials

Reaction	$E^{\ominus}$/V (vs. NHE)
$CO_2\ (g) + 8H^+ + 8e^- \rightarrow CH_4\ (g) + 2H_2O$	−0.24
$CO_2\ (g) + 6H^+ + 6e^- \rightarrow CH_3OH\ (aq) + H_2O$	−0.38
$CO_2\ (g) + 4H^+ + 4e^- \rightarrow HCHO\ (aq) + H_2O$	−0.48
$CO_2\ (g) + 2H^+ + 2e^- \rightarrow CO\ (g) + H_2O$	−0.52
$CO_2\ (g) + 2H^+ + 2e^- \rightarrow HCOOH\ (aq)$	−0.61
$CO_2\ (g) + 2H^+ + 2e^- \rightarrow H_2C_2O_4\ (aq)$	−0.90
$CO_2\ (g) + e^- \rightarrow *CO_2^-$	−1.90

The presence of protons is crucial in facilitating the catalytic reduction process, ultimately leading to the generation of valuable chemicals containing one or more carbon atoms. However, the transfer mechanism and promoting effect of protons in photocatalytic CO_2 reduction still require further in-depth research. Unlike previous catalytic reactions, which are often conducted in acidic environments provided by HI, water offers mild and low-cost reaction conditions and serve as an ideal proton donor. *In situ* Fourier transform infrared (FT-IR) spectroscopy has been widely used to detect the intermediates produced during photocatalytic CO_2 reduction. Extensive characterization data shows that, after CO_2 molecules are activated by the catalyst, protons from water protonate them to form $*COOH^-$, which has a lower formation energy and serves as a key intermediate for conversion to CO.

This intermediate can be further protonated to produce *CHO, which is then converted into CH_4 with high fuel value through a series of steps, including dimerization [44]. Moreover, if *CO intermediates remain in the system and the reaction energy barrier for C-C coupling is effectively reduced, *CO and *CHO will play a crucial role in forming the key intermediate *OC-CHO, potentially leading to the production of C_2H_5OH or C_2H_6, both of which have higher industrial value [45]. Therefore, protons transferred to the catalytic active sites are pivotal for the formation of catalytic products.

For an ideal photocatalyst used in CO_2 reduction, the conduction band potential should be higher, and the valence band potential should be lower than the standard redox potentials of the reduction products, such as CO, CH_4, and HCHO. In other words, the band gap of the semiconductor must be wide enough to trigger photocatalytic redox reactions. However, if the bandgap is too large, the ability to utilize sunlight effectively will be limited. Recent studies have indicated that the optimal bandgap for semiconductors used in photocatalysis typically ranges from 1.8 to 2.8 eV [7,46].

Figure 2 illustrates some photocatalysts that meet these criteria and exhibit superior CO_2 reduction capabilities. On the other hand, an excessively small bandgap is also undesirable because it increases the likelihood of free electrons and holes recombining during their diffusion to the semiconductor surface. This recombination process causes the electrons and holes to return to their ground states, releasing energy. Generally, carrier recombination can occur through two mechanisms: radiative recombination and non-radiative recombination. It is clear that photogenerated electrons and holes would be consumed during the recombination process, which is detrimental to the progression of the photocatalytic

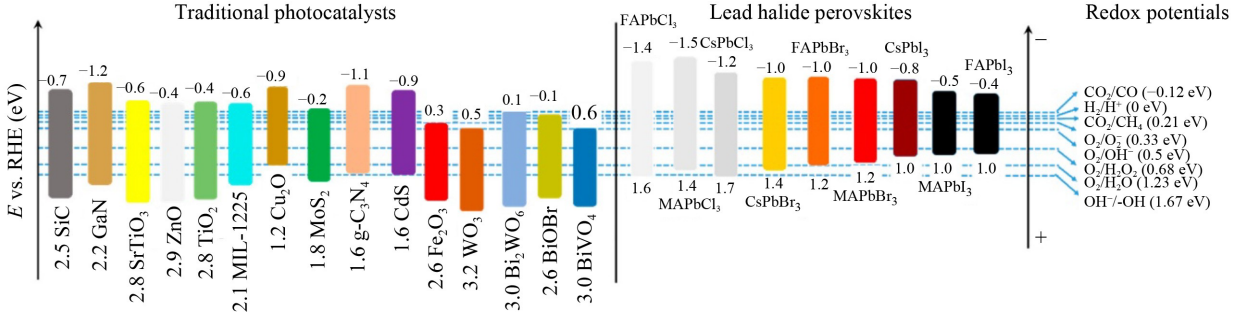

Fig. 2 Band energy positions of photocatalysts (vs. NHE) and the redox potential of some half-reactions (adapted from Huang et al. [33] under the terms of CC BY-NC 4.0 license).

reaction [47]. However, this issue can be mitigated in semiconductors with fewer intrinsic defects, allowing the reaction to favorably proceed toward the desired redox reactions [1].

The concept of "defect tolerance" refers to the property by which, even in materials with a high density of defects, the energy levels are generally not positioned within the band gap but are instead confined to the conduction or valence band [48–50]. This property enables metal halide perovskites (MHPs) to achieve a high carrier utilization rate, thereby enhancing their photocatalytic performance. For example, in the typical lead halide perovskite material $APbX_3$, the band gap is dominated by the antibonding orbitals of Pb and halogen atoms (Fig. 3) [50]. The energy level of the defect is allowed to fall within either the conduction band or the valence band, not within the band gap itself. The term "shallow states" has been used to highlight this phenomenon, which has the potential to facilitate charge separation, making charge carrier utilization more efficient for such materials, and ultimately improving photocatalytic performance [49]. Over the past few years, MHPs have proven to be highly efficient photo-driven catalysts, emerging as novel cutting-edge materials in many solar driven applications [32,33,36,37,51–55].

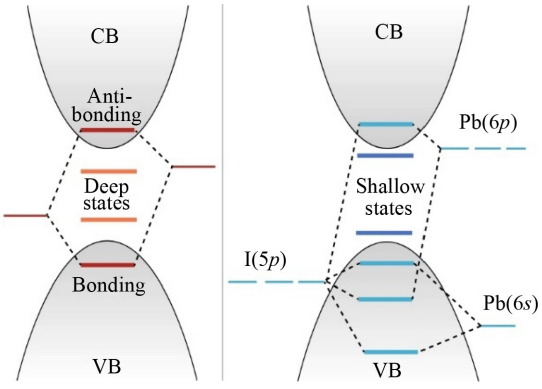

Fig. 3 Electronic structure of defect intolerant semiconductors (left) and defect tolerant materials (right) (adapted with permission from Brandt et al. [50], copyright 2017, American Chemical Society).

3 Synthetic strategies of metal halide photocatalysts

Developing simple and effective synthesis strategies is an important prerequisite for broader application of metal halide photocatalysts. Several synthesis methods with flexible control of reaction conditions have been reported for the preparation of metal halide photocatalytic materials with different physicochemical properties [56–59]. These properties include factors such as composition, morphology, and more [60]. This section focuses on the widely used methods— hydrothermal, hot injection, ligand-assisted reprecipitation (LARP), and anti-solvent precipitation—for the synthesis of metal halide photocatalysts.

3.1 Hydrothermal method

The hydrothermal method is one of the most widely used techniques for synthesizing crystalline materials. Typically, the precursors are added as reactants with water serving as the reaction medium in a specially designed sealed vessel, such as an autoclave. By heating the reaction vessel, a high-temperature (100–1000 °C) and high-pressure (1.0–100 MPa) environment is created, allowing the insoluble powder reactants to dissolve and recrystallize (as shown in Fig. 4(a)) The crystals prepared by the hydrothermal method usually has the characteristics of well-developed grains, small particle sizes, and uniform distribution. Moreover, this method allows the use of inexpensive raw materials and facilitates the formation of desired stoichiometry and crystal structures. These unique advantages have made the hydrothermal method widely applicable in active research areas such as material synthesis, chemical reactions, and chemical treatments.

For instance, in 2024, Yin et al. [61] conducted the first systematic study of the TJU-39(Pb) and TJU-40(Pb/TM, TM = Co^{2+}/Ni^{2+}) series of photocatalysts, which feature layered PbI_2 and three-dimensional (3D) transition metal intercalates. These photocatalysts demonstrated high efficiency in the solar-driven conversion of CO_2 to ethanol. In their synthesis, water and a small amount of perchloric acid were added to a Teflonlined autoclave reactor containing the precursors of PbI_2 and disodium iminodiacetate (imi), which was then heated in an oven at 160 °C for 48 h. After naturally cooling to room temperature, yellow plate-like crystals, TJU-39(Pb) were obtained by filtration and washed alternately with H_2O and DMF three times. The synthesis of TJU-40(Pb/TM) followed the same procedure as TJU-39(Pb), with the addition of a certain molar ratio of $TM(OAc)_2$. As-prepared resultants achieved efficient photocatalytic conversion of CO_2 to C_2H_5OH with the evolution rates of 24.9–31.4 μmol/(g·h), and selectivity exceeded 90%. As described above, the hydrothermal method is a practical technique for synthesizing metal halide photocatalytic crystals.

3.2 Hot-injection (H-I)

From the perspective of liquid-phase synthesis, the heat-injection (HI) method is widely used because it avoids the use of polar solvents and enables the synthesis of high-quality MHP materials through dispersed particles [1]. In this method, a completely dissolved precursor is rapidly injected into a hot solution containing raw

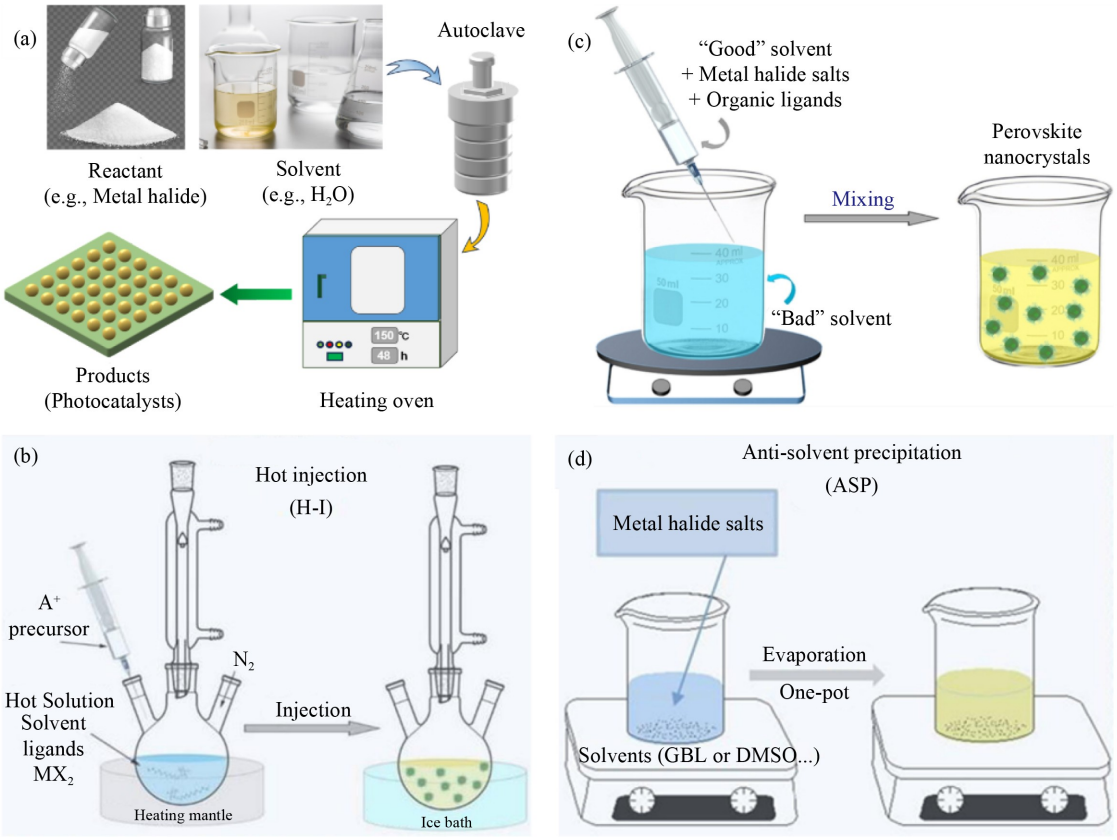

Fig. 4 Diagrammatic sketch.

(a) Hydrothermal method; (b) hot injection (adapted with permission from Wang et al. [1], copyright 2020, Elsevier B.V. and Science Press); (c) LARP (adapted from Shamsi et al. [60] under the terms of CC BY-NC 4.0 license); (d) anti-solvent precipitation methods (adapted with permission from Ref. [1], copyright 2020, Elsevier B.V. and Science Press).

materials such as organic ligands and high-boiling solvents (see Fig. 4(b)). Conducting the process in a nitrogen atmosphere helps protect the synthesized material from degradation due to exposure to air, and the procedure also includes a degassing step. In 2024, Chen and colleagues reported the synthesis of a lanthanide (Ln^{3+})-doped layered double perovskite nanocrystal, $Cs_4M(II)Sb_2Cl_{12}$ (M(II): Cd or Mn), where Ln^{3+} can be Yb^{3+} or Er^{3+} [62], enabling efficient near-infrared (NIR) photoluminescence. Similarly, Han and other researchers reported that zero-dimensional (0D) Cs_3BiCl_6, $Cs_3Bi_2Cl_9$ and $Cs_4MnBi_2Cl_{12}$ nanosheets (NSs) can be synthesized using the H-I method, providing valuable insights into the application of bismuth-based halide perovskite materials in radiation detection [62]. By tuning different reaction temperatures, different volumes of crystals can be obtained, which is quite satisfactory. However, the thermal injection method has certain drawbacks, including the requirement for high temperatures, an inert atmosphere, and a low repetition rate, all of which limit its large-scale industrial application [63]. To address these issues, ligand-assisted reprecipitation (LARP) offers a more cost-effective solution, enabling the synthesis of high-quality metal halides at room temperature and pressure [64].

3.3 LARP

LARP synthesis of metal halide crystals involves using organic ligands in non-polar solvents (commonly hexane, toluene, etc.), while precursor salts such as lead halide, stannous halide, and others are dissolved in polar solvents (usually DMF, DMSO, etc.). When these two systems with different polarities are mixed, the solute becomes instantaneously supersaturated due to the polarity change, leading to spontaneous precipitation and crystallization. This promotes the nucleation and growth of MHP nanocrystals (Fig. 4(c)). It is evident that LARP allows for precise control over crystal size at the nanometer level. Rtimi and his colleagues synthesized organic-inorganic halide perovskite $MAPb_{1-x}Zn_xBr_{3-2x}Cl_{2x}$ nanocrystals using LARP [65], reducing the material's toxicity by incorporating Zn^{2+}. In 2023, Dhakal et al. [66] first synthesized orthogonal perovskite nanocrystals, $CH(NH_2)_2SnI_3$, with an average diameter of 7.7 nm and low toxicity via LARP. These nanocrystals demonstrated high stability for at least 265 days at room temperature and 20% relative humidity in an N_2 atmosphere. Given

the simplicity of the required equipment, LARP shows great potential for large-scale production of metal halide nanocrystals, generating significant excitement in the field.

3.4 Anti-solvent precipitation (ASP)

The traditional H-I [67,68] and LARP methods [69–71] enable precise control over the size and morphology of MHPs [72]. Nonetheless, these methods are not suitable for large-scale synthesis of MHPs, limiting their industrial application. To address this limitation, the anti-solvent precipitation (ASP) method has been developed (Fig. 4(d)) [1], offering advantages such as environmental friendliness, low cost, and simplicity [73–76].

Generally, the ASP method involves the following steps: the precursors are dissolved in an organic solvent (such as DMF or DMSO) to form an organic phase, followed by the addition of an anti-solvent, such as chlorobenzene or isopropanol. The solution is then heated and evaporated to achieve supersaturation, effectively separating the components between the solvent and the anti-solvent. Finally, MHP crystals precipitate as the solution cools. For example, Tang et al. successfully synthesized highly stable $CsAgCl_2$ crystals utilizing DMSO and isopropanol via the ASP method [77]. The obtained crystals possess excellent stability under air, heat, and light, along with outstanding performance in photocatalytic CO_2RR. The ASP method enhances the interfacial contact between MHPs and reaction substrates, thanks to its rapid growth kinetics that facilitate the reaction. As a result, MHPs are directly generated on the substrate surface. Other photocatalysts synthesized using the ASP approach include $MAPbI_3$ (MA^+=methylammonium) [78], $CsCuCl_3$ [79], and Cs_2PdBr_6 [80]. While the ASP method is simple and easy to implement, it has inherent disadvantages, such as the production of micrometer-scale crystals and low crystallinity, which may have a negative impact on the photocatalytic performance of the materials.

4 Structural engineering strategies of metal halides for photocatalytic CO_2RR

With outstanding physical properties and specific chemical structure, metal halide-based photocatalysts have been successfully developed and increasingly utilized in the field of solar energy conversion into clean energy. These materials have shown promising applications in CO_2 photoreduction, photocatalytic H_2 evolution reaction (HER), photocatalytic degradation of organic pollutants, and the synthesis of organic compounds [81,82]. However, the separation of photogenerated electron-hole pairs competes with recombination processes, which limits the efficiency of these systems [83–85]. Furthermore, CO_2 reduction is a complex reaction that produces multiple products, with the yield of the target product being influenced by proton reduction processes. Therefore, it is crucial to understand the dynamics of photogenerated carriers and fully elucidate the mechanisms behind CO_2 reduction reactions.

4.1 All-inorganic metal halide perovskite photocatalysts

Among all inorganic metal halide perovskite photocatalysts, $CsPbBr_3$ (CPB)-based materials have been the most widely studied. Recently, CPB has become a research hotspot for photocatalytic applications due to its suitable bandgap, long electron-hole diffusion length, and excellent photoresponsivity [86,87]. CPB quantum dots (QDs) were first reported by Kuang et al. in 2017 for photocatalytic CO_2 conversion into chemical fuels (Fig. 5(a)) [88]. The structure of CPB exhibits a typical octahedral shape, with Cs^+ occupying the A-site and positioned at the vertices of the shared surface, as shown in Fig. 5(b) [89]. Ethyl acetate (EA), with mild polarity, was selected as both the solvent and sacrificial agent, maximizing CO_2 dissolution while maintaining the stability of CPB. Under AM 1.5G simulated sunlight irradiation, CO_2 was reduced to CO and CH_4 at a rate of 23.7 mmol/(g·h), and the product selectivity reached to 99.3%.

When the semiconductor is processed into different nanostructures, both the surface and electronic structure of the material change, which in turn affects surface reactivity and band structure [90]. Meanwhile, adding an appropriate amount of water to the reaction system can reduce H_2 production and enhance the selectivity of CO_2 reduction [91]. However, excessive water intake negatively impacts the stability of PQDs. Subsequently, Sun and colleagues demonstrated that the bandgap, carrier lifetime, and electron-hole separation efficiency of CPB QDs (3–12 nm) are largely size-dependent [92]. If the size of QDs is too large, the surface area decreases, while if it is too small, aggregation occurs. The performance of CPB PQDs with four different sizes in the EA/H_2O environment for CO_2 reduction was compared, with the highest PQD yield observed at 8.5 nm after 8 h of sunlight irradiation (see Fig. 5(c)).

Later, Chen et al. combined CPB perovskite NCs with a hybrid transition metal complex, Ni(tpy), and efficiently promoted the photocatalytic reduction of CO_2 to CO and CH_4 (Fig. 5(d)) [93]. Under irradiation of simulated light from a 300 W Xenon lamp (λ > 400 nm), the total production of CO and CH_4 reached 431 μmol/(g·h). The catalytic activity for CO and CH_4 production under monochromatic light at 450 nm was 26 times higher than that of pristine CPB. High stability was confirmed by its performance over 16 h. It is evident that the introduction of Ni(tpy) provides more catalytic sites for CO_2 reduction, thus enhancing catalytic performance.

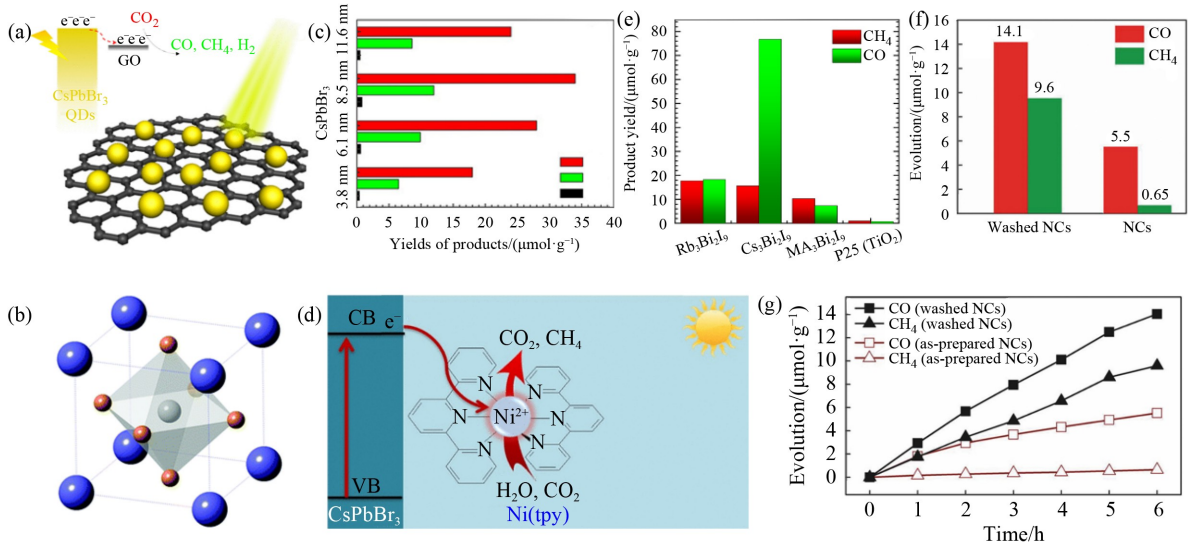

Fig. 5 Structural design, catalytic mechanism, and performance comparison of typical all-inorganic metal halides perovskite photocatalysts for photocatalytic reduction of CO_2.

(a) Schematic illustration of $CsPbBr_3$-QD/GO photoreduction of CO_2 (adapted with permission from Xu et al. [88], copyright 2017, American Chemical Society); (b) crystal structure of $CsPbBr_3$, where the blue, gray and brown atoms represent Cs, Pb and Br, respectively (adapted from Wei et al. [89] under the terms of CC BY 3.0 license); (c) photoreduction of CO_2 over $CsPbBr_3$ QDs with different sizes (adapted with permission from Hou et al. [92] , copyright 2017, Wiley-VCH Verlag GmbH & Co. KGaA, Weinheim); (d) schematic illustration of the $CsPbBr_3$-Ni(tpy) catalytic system for photoreduction of CO_2 (adapted with permission from Chen et al. [93] , copyright 2020, American Chemical Society); (e) yields of CO and CH_4 production in different Bi-based samples (adapted with permission from Bhosale et al. [94], copyright 2019, American Chemical Society); (f) CO and CH_4 formation; (g) times course product formation in different samples of CABB (adapted with permission from Zhou et al. [96] , copyright 2018, Wiley-VCH Verlag GmbH & Co. KGaA, Weinheim).

Unfortunately, the toxicity of Pb has always been a major factor limiting the wide application. Compared with the less stable Sn-based perovskites, Bi-based materials have proven to be the best substitutes. Bhosale et al. developed a series of non-toxic Bi-based halide perovskite materials, $Rb_3Bi_2I_9$ and $Cs_3Bi_2I_9$ [94]. These catalysts maintained 12-h working stability after UV irradiation for up to 7 days, as confirmed by XRD results. Under UV light (λ = 305 nm) for the same time, the production of CO followed the order: $Cs_3Bi_2I_9$ > $Rb_3Bi_2I_9$ > P25 TiO_2, while the catalytic activity toward CH_4 followed this order: $Rb_3Bi_2I_9$ > $Cs_3Bi_2I_9$ > P25 TiO_2 (Fig. 5(e)). Two years later, Lu et al. reported pure antimony-based lead-free perovskite NCs, $Cs_3Sb_2Br_9$ [95]. $Cs_3Sb_2Br_9$ NCs showed a 10-fold enhancement in CO_2 reduction to CO activity, generating 510 μmol/g of CO in 4 h, compared to $CsPbBr_3$. This enhancement is attributed to the Sb active sites on the surface of $Cs_3Sb_2Br_9$, which efficiently generate *COOH and *CO intermediates, as supported by DFT calculations.

Different from $CsPbBr_3$-based materials, other MHPs containing multiple metal components have also been reported, such as the two-component perovskite with the general formula $A_2B_1^+B_2^+X_6$ [97,98]. Notably, the lead-free and highly crystalline $Cs_2AgBiBr_6$ (CABB) NCs [56,96,99], synthesized by Zhou et al. in 2018 using a common heat injection method, exhibit a high degree of stability, remaining intact for 3 weeks in mild or non-polar solvents. Methods to reduce ligand density by washing with absolute ethanol have been proposed to improve catalytic performance. XPS and Fourier Transform Infrared Spectrometer (FTIR) characterization results confirmed that the surface ligands could be completely washed away, and Thermogravimetric Analysis (TGA) results showed that the organic residues were also cleaned. The catalytic activity of washed CABB NCs for CO_2 reduction was greatly enhanced after 6 h, with increased CO and CH_4 production (Figs. 5(f) and 5(g)).

Up to present, increasing attentions have been paid to the development of lead-free biphasic halide perovskite photocatalysts, with a focus on both high stability and catalytic efficiency. Among these, $Cs_2InSbCl_6$ and $Cs_2InBiCl_6$ [100] have also been reported. Their suitable bandgap, low exciton binding energy, and high stability make them ideal candidates for the most promising lead-free halide perovskite photocatalysts, providing invaluable insights for the study of lead-free halides in photocatalysis.

4.2 All-inorganic metal halide non-perovskite photocatalysts

In all-inorganic metal halides, some non-perovskite compounds have attracted attention due to their excellent

stability and photocatalytic performance. Currently, bismuth-based oxyhalide materials, known for their crystal tunability and compositional structure that significantly influence photocatalytic performance, have attracted extensive research [101,102]. For instance, Wang et al. [103] synthesized Bi_5O_7I nanosheets with porous structure from the parent material $BiOIO_3$ through high-temperature calcination, exhibiting enhanced photo-responsivity properties.

Unlike the aforementioned perovskite structure, it is evident that, as a non-perovskite photocatalyst, the inorganic components are no longer arranged in a regular octahedral form (see Fig. 6(a)) [104]. The robust CO_2 reduction activity is attributed to the more efficient adsorption and activation of CO_2 molecules on the surface of Bi_5O_7I (E_{ads} = − 0.27 eV), as demonstrated by *in situ* diffuse reflectance infrared Fourier transform spectroscopy (DRIFTS), DFT calculations, and other experimental analyses. The high photocurrent response of Bi_5O_7I indicates efficient charge separation and transfer, which is further supported by the significantly reduced photoluminescence (PL) intensity, suggesting a lower likelihood of electron-hole recombination.

Under visible light irradiation (λ > 420 nm), CO was

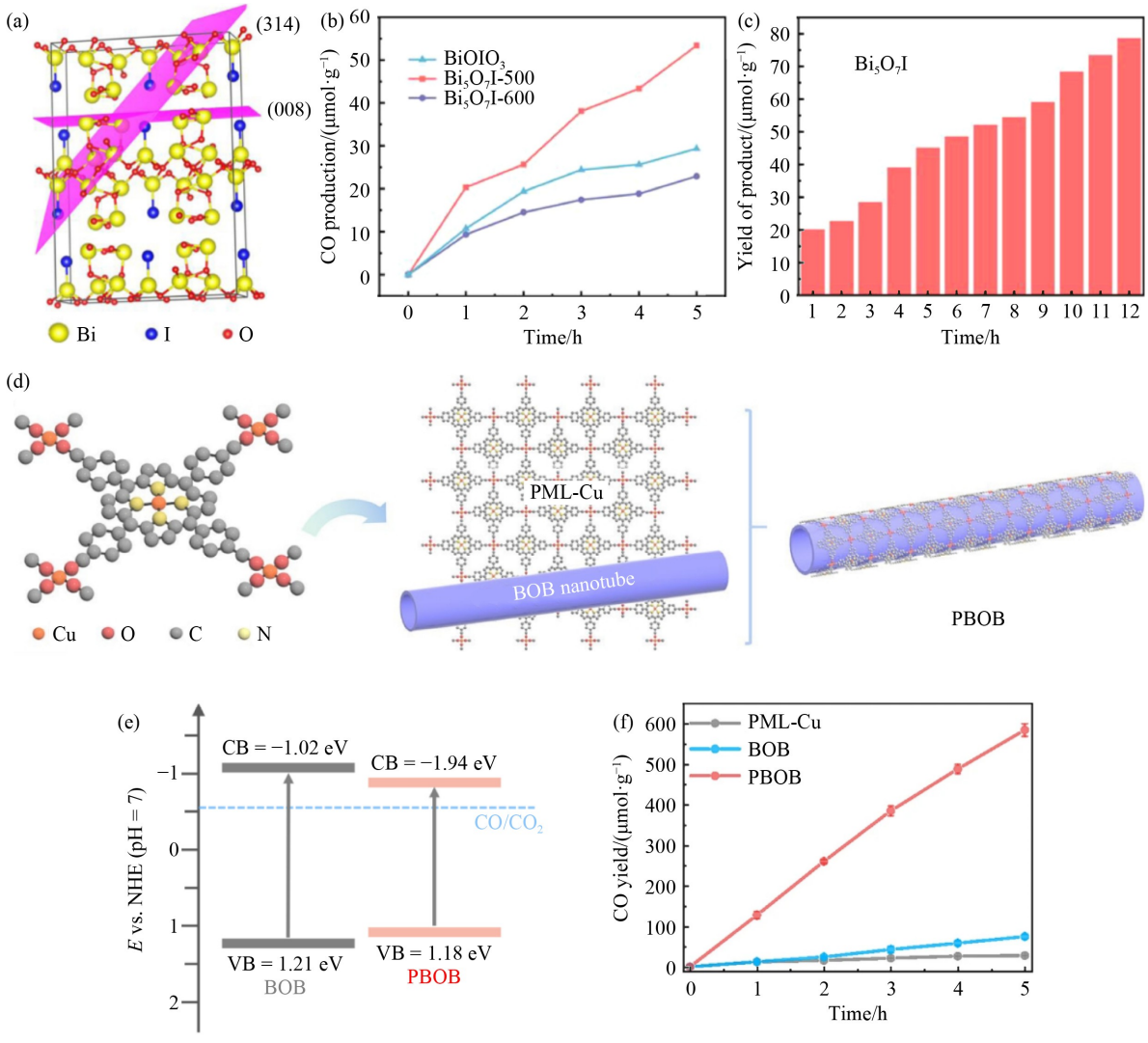

Fig. 6 Design, synthesis, and CO_2 photoreduction properties of all-inorganic non-perovskite photocatalysts and their composites focus on structure-energy band regulation and interfacial activity optimization.

(a) Molecular and crystal plane model of Bi_5O_7I (adapted with permission from Li et al. [104], copyright 2021, Elsevier B.V.); (b) CO generation for as-prepared samples (adapted with permission from Wang et al. [103], copyright 2023, Elsevier B.V.); (c) yields of CO evolution over time in wet CO_2 by Bi_5O_7I-500 (adapted with permission from Wang et al. [103], copyright 2023, Elsevier B.V.); (d) description of synthesis of composite material PBOB (adapted from Zhang et al. [105] under the terms of CC BY license); (e) band structure of BOB and PBOB (adapted from Zhang et al. [105] under the terms of CC BY license); (f) time-dependent production of CO by photocatalytic CO_2 reduction using as-synthesized PBOB, BOB and PML-Cu as the catalyst (adapted from Zhang et al. [105] under the terms of CC BY license).

the only product observed, with a yield of 10.67 μmol/g, nearly twice that of the parent material (Fig. 6(b)). In a 12-h long-term illumination experiment, CO production showed a roughly linear growth trend, and no signs of deactivation were observed in the photocatalysts (Fig. 6(c)), demonstrating good stability.

Unfortunately, the precise regulation of the state and number of active centers, along with the charge transfer process, remains a limiting factor for further applications due to the influence of the contact interface [106]. To develop catalysts with high-density active sites, Li et al. employed a strain-induced strategy to polarize the dual surface interface. By using strain engineering, they successfully assembled a Cu porphyrin-based atomic layer (PML-Cu) with $Bi_{12}O_{17}Br_2$ (BOB), resulting in the formation of PML-Cu/$Bi_{12}O_{17}Br_2$ (PBOB) (Fig. 6(d)), triggering a multi-step polarization process at the surface interface [105]. The work function (Φ), calculated via ultraviolet photoelectron spectroscopy (UPS), indicates that the electrons in BOB tend to flow toward PML-Cu, creating an internal electric field (IEF) [107]. This IEF accelerates the polarization of the interface in PBOB, enhancing the electron transfer between the layers. The local polarization field disrupts charge symmetry, promoting the effective separation of photogenerated electrons and holes [108,109].

XPS valence band spectra revealed that the VB of BOB and PBOB were 1.21 and 1.18 eV, respectively. Combined with UV-vis spectral data, the CB of the two were inferred to be −1.02 and −0.94 eV, respectively (Fig. 6(e)). The band structure implies that the interface-polarized PBOB can be used for CO_2 photoreduction to CO, as validated by photocatalytic CO_2 reduction performance tests. In these experiments, the only carbon containing product, CO, was precipitated in PBOB with a yield of 584.3 μmol/g after 5 h (Fig. 6(f)), achieving performance that was 7.83 and 21.01 times higher than that of BOB and PML-Cu, respectively. The catalytic activity of PBOB remained at 90.60% after 5 cycles, demonstrating that the as-polarized samples exhibit robust stability.

It is worth noting that H_2O_2 was detected alongside CO_2 reduction as a highly practical photocatalytic oxidation product. After the reaction, the content of H_2O_2 can reach 63.80 μmol/g in the solution. This suggests that the induced surface interface dual polarization strategy can effectively address the issues of limited active sites and slow charge transfer in photocatalysts, highlighting its potential for designing photocatalysts with concentrated active sites.

In a similar study, Gong et al. [110] used oxygen vacancies (OVs) and bismuth clusters to assist $Bi_{12}O_{17}Cl_2$ nanosheets in achieving efficient and selective CO_2 photoreduction. The hydrothermal method was employed to prepare OV-rich and bismuth-rich ultrathin nanosheets, with OV-poor and bismuth-poor $Bi_{12}O_{17}Cl_2$ samples prepared for comparison. The synthesized multifunctional OV-Bi-$Bi_{12}O_{17}Cl_2$ exhibited a CO release rate of 64.3 μmo/(g·h), which was 15 times higher than that of the OV-poor sample. In addition, this performance is significantly improved by 28 times compared to bulk $Bi_{12}O_{17}Cl_2$ (2.3 μmol/(g·h)), as shown in Fig. 7(a). Remarkably, similar CO yields were maintained over four consecutive cycles without any structural or morphological changes, demonstrating the excellent photocatalytic activity and stability of OV-Bi- $Bi_{12}O_{17}Cl_2$ (Fig. 7(b)). It is suggested that OV can impart a negative charge to $Bi_{12}O_{17}Cl_2$, creating electron trapping sites that promote the adsorption and activation of CO_2. Additionally, the Bi clusters act as photohole receptors, and the synergistic effect of the OV and Bi clusters enhances carrier transfer, improving charge separation efficiency and offering potential advantages for subsequent photoreduction.

In a more recent study, Yang and colleagues anchored Co atoms onto ultra-thin BiOCl single-crystal nanosheets using hydrothermal and sintering engineering techniques. XRD, Raman spectroscopy, and TEM characterizations confirmed the successful synthesis of these materials [111]. The addition of polyvinylpyrrolidone (PVP) inhibited the stacking of [Cl^-Bi-O_2-BiCl] units between layers, preserving the ultrathin nanosheet morphology. The introduction of Co atoms enhances electron delocalization around Bi-O and Co-O bonds, promoting electron transfer. Simultaneously, the conduction band of the material exhibits a noticeable downward shift, improving electron mobility. These findings are supported by the density of states (DOSs) calculations. Compared to the typical two-dimensional indirect semiconductor BiOCl, the as-synthesized 2Co-BiOCl enhances the average CO generation rate by approximately 13 times, reaching 183.9 μmol/(g·h) (Fig. 7(c)). A series of control experiments-conducted without light, water, or the photocatalyst, confirmed that the CO generated originates from the photocatalytic reduction of CO_2 and water, demonstrating that this process is indeed photo-driven. To highlight the uniqueness and advantages of Co-BiOCl materials, the performance of 2Co-BiOCl was compared to that of other reported bismuth-based catalysts. Remarkably, the catalytic performance of 2Co-BiOCl ranks among the best, positioning it as an efficient and stable candidate for carbon reduction applications (Fig. 7(d)).

4.3 Organic-inorganic hybrid metal halide perovskite photocatalysts

In recent years, metal halide perovskites have become a focal point in photocatalytic CO_2RR research, offering unique advantages such as excellent carrier mobility and tunable bandgaps [112–116]. When combined with metal-organic frameworks (MOFs), their CO_2 reduction

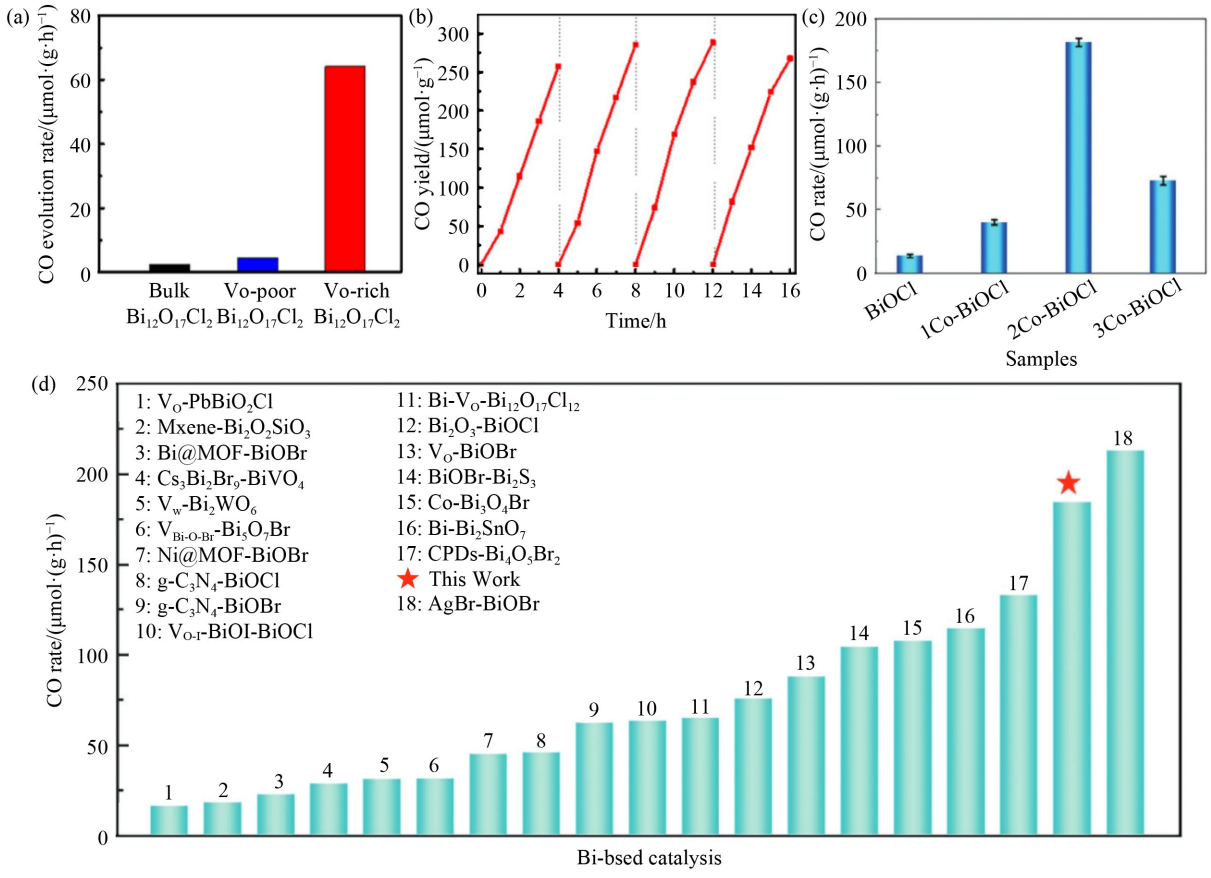

Fig. 7 Investigation of the impact of environmentally friendly bismuth-based halide non-perovskite photocatalysts on photoreduction CO_2 conversion applications.

(a) CO production rate; (b) photocatalytic stability of OV-rich Bi–$Bi_{12}O_{17}Cl_2$ nanosheets ((a) and (b) adapted from Guan et al. [110] under the terms of CC BY-NC 4.0 license); (c) CO yield rate of as-obtained samples; (d) performance comparison of 2Co-BiOCl and Bi-based catalysis (adapted with permission from Zhao et al. [111] , copyright 2024, Wiley-VCH GmbH).

efficiency has been significantly enhanced [117]. However, the widespread use of metal halide perovskite is still limited, primarily due to their low conversion efficiency and stability [118]. To address these challenges, one promising strategy involves introducing organic compounds to replace the ions at A sites in the perovskite structure. Que et al. reported that colloidal $FAPbBr_3$ QDs, which exhibit a lower carrier recombination rate and high thermal, optical, and water stability, can effectively overcome these difficulties (Fig. 8(a)) [119]. The high crystallinity cubic samples (Fig. 8(b)) were prepared by the H-I method. $FAPbBr_3$ crystallizes in a cubic system, with six halogen anions located at the corners and center of the cube, respectively. These anions interconnect with Pb ions at the center of the unit cell, forming a well-structured octahedral three-dimensional skeleton, characteristic feature perovskite catalyst. Compared to traditional $CsPbBr_3$ QDs, $FAPbBr_3$ QDs have a broader absorption spectrum and retain 40% of their fluorescence intensity after 520 min of irradiation in a deionized water (DI)/ethyl acetate (EA) environment. Under 300 W Xenon arc lamp irradiation in DI/EA, $FAPbBr_3$ QDs achieved a CO yield of 181.25 μmol/(g·h), with an electron consumption ($R_{electron}$) of 504.44 μmol/(g·h), accompanied by a small amount of CH_4. The CO_2 selectivity exceeded 97%, effectively inhibiting the hydrogen evolution reaction (HER) in this process.

The first top-down synthesis of $MA_3Bi_2I_9$ by Diau and colleagues provides a benchmark strategy for preparing non-toxic and stable photocatalysts for the photoreduction of CO_2 to high-value fuels like CH_4 [94]. The isolated $[Bi_2I_9]^{3-}$ ion in $MA_3Bi_2I_9$ supports its zero-dimensional structure, which effectively preserves the octahedral configuration typical of perovskite, thanks to the formation of the face-sharing Bi-I bonds [120]. The photoreduction stability of the synthesized sample was confirmed by maintaining the XRD pattern adequately after one week at 70% RH, followed by 12 h of continuous ultraviolet irradiation. UPS data provides direct evidence that $MA_3Bi_2I_9$ nanocrystals (NCs) are suitable for CO_2RR, with their energy levels between −5.29 and −2.89 eV, aligning with the reduction potentials of CO_2/CO and CO_2/CH_4 at −3.97 and −4.26 eV, respectively (Fig. 8(c)). The photoreduction

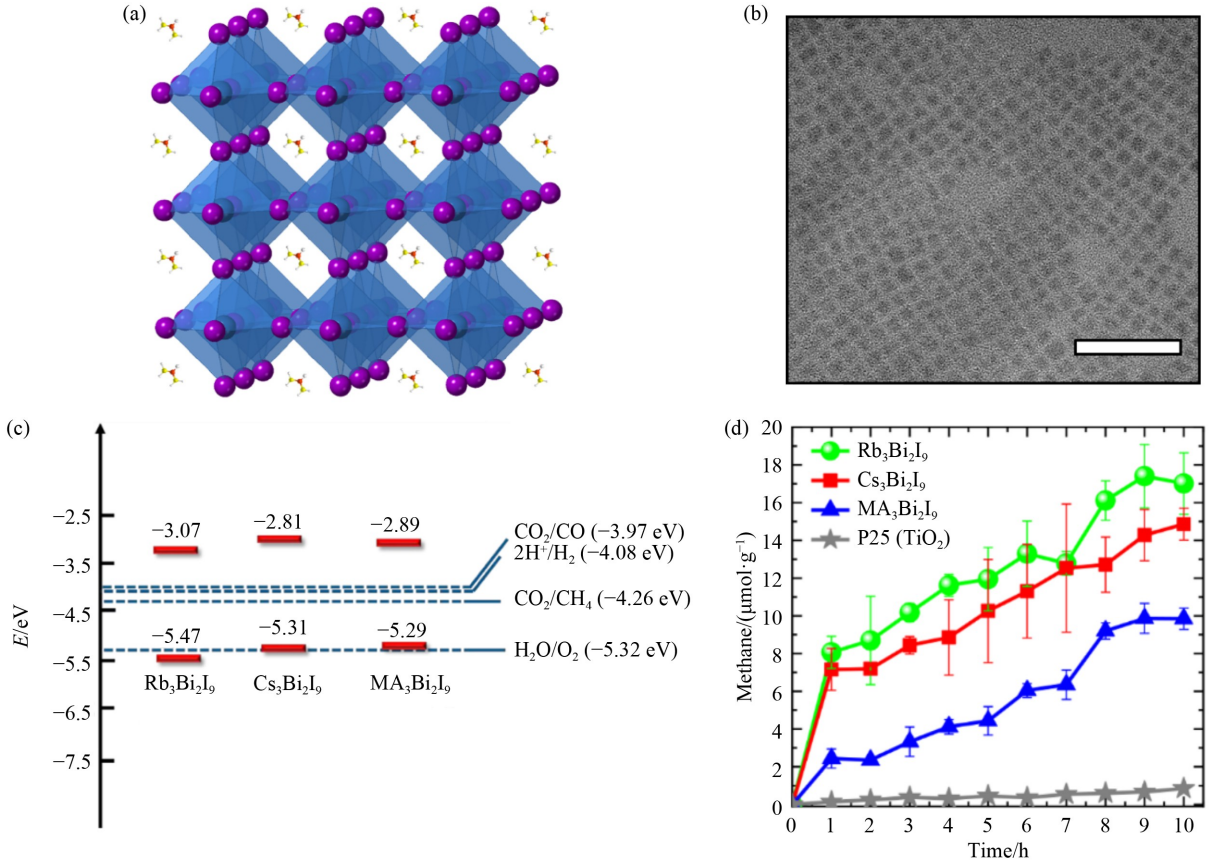

Fig. 8 Comprehensive characterization of organic-inorganic hybrid lead halide perovskite materials and performance evaluation of as-reported bismuth-based photocatalysts.

(a) Schematic diagram of the crystal structure (adapted with permission from Que et al. [119], copyright 2020, Elsevier); (b) TEM image of $FAPbBr_3$ perovskite (adapted with permission from Que et al. [119], copyright 2020, Elsevier); (c) potential-energy levels (versus vacuum) of bismuth-based photocatalysts (adapted with permission from Bhosale et al. [94], copyright 2019, American Chemical Society); (d) methane yields of as- prepared bismuth-based materials (detected with GC-FID) (adapted with permission from Bhosale et al. [94], copyright 2019, American Chemical Society).

experiment demonstrated that $MA_3Bi_2I_9$ NCs could generate CH_4 at a yield of approximately 10.4 μmol/g, while CO was produced at a yield of 7.2 μmol/g, as detected by gas chromatography-mass spectrometry (GC-MS). Mechanistic studies indicate that A-site cations and crystal structure significantly affect the catalytic activity of photocatalysts. Notably, the yield of both products in the organic-inorganic hybrid sample is lower than that of the all-inorganic photocatalyst prepared using the same method (Fig. 8(d)). This may be attributed to the stabilization of holes in $MA_3Bi_2I_9$ by Bi^{4+}, $\bullet CH_2NH_3^+$ radical cations, and oxygen anions, which reduces the efficiency of hole transfer to the desired oxidation channel. The quenching of the electron paramagnetic resonance (EPR) signal in the MA-based material diminishes, weakening the catalytic performance of $MA_3Bi_2I_9$ compared to the other two inorganic cation NC catalysts.

Ultimately, bismuth-based photocatalysts offer key advantages such as a wide bandgap, high binding energy, and non-toxicity, making them promising candidates for various optoelectronic applications.

Improving the stability of organic-inorganic hybrid lead halide perovskite materials in polar solvents is crucial for enhancing CO_2 conversion in practical applications. One effective approach involves designing MOFs to encapsulate perovskites, providing protection similar to a cage around the metal halide perovskites (MHPs). Specifically, the composite photocatalyst $MAPbI_3$@PCN-221(Fe_x) (where $x = 0 - 1$), was successfully fabricated by sequentially depositing the classical lead halide perovskite $MAPbI_3$ QDs within an iron porphyrin MOF, as reported by Lu et al. [116]. The structure of $MAPbI_3$ is illustrated in Fig. 9(a) [121]. The results show that when $x = 0.2$, CO and CH_4 were produced by $MAPbI_3$@PCN-221($Fe_{0.2}$) under 300 W Xe-lamp irradiation, achieving a high total yield of 1559 μmol/g, which is 38 times higher than that from the original PCN-221($Fe_{0.2}$), which was only 41 μmol/g. A continuous reaction lasting 80 h demonstrated a significant improvement in stability of the composite, as shown in Figs. 9(b) and 9(c). The reaction, conducted in

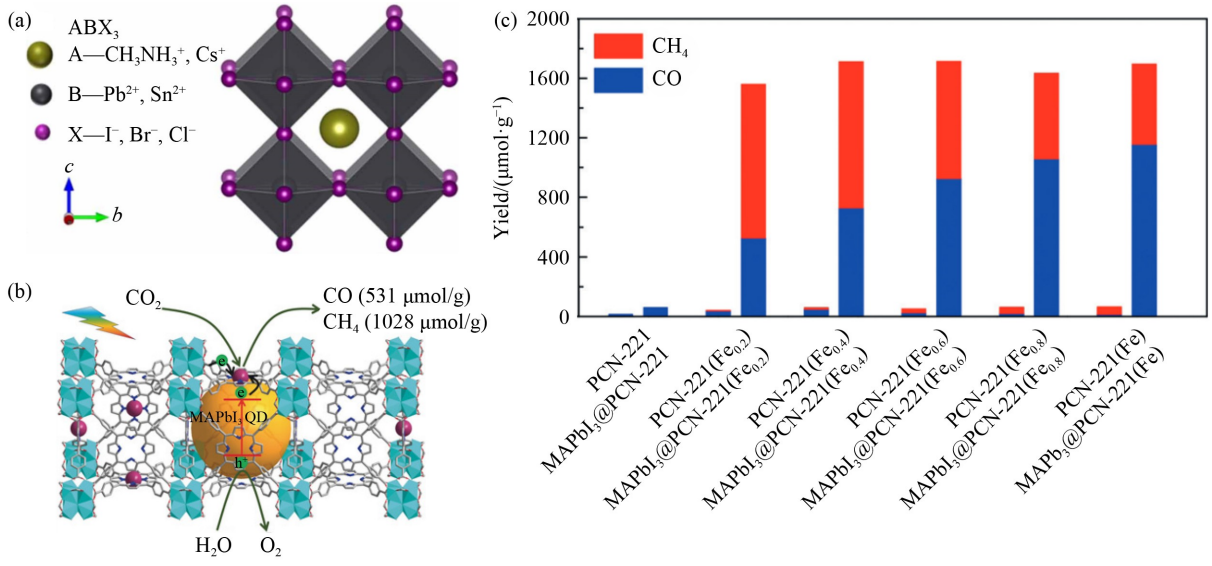

Fig. 9 An overview of key information pertaining to $MAPbI_3$ perovskite materials.

(a) Typical crystal view of $MAPbI_3$ perovskites (adapted from Xiao et al. [121] under the terms of CC BY-NC 4.0 license); (b) encapsulation of $MAPbI_3$ quantum dots in porous PCN-221 (Fe_x) (adapted with permission from Wu et al. [117], copyright 2019, Wiley-VCH Verlag GmbH & Co. KGaA, Weinheim); (c) yields of CO and CH_4 of the photocatalytic products of the as-obtained photocatalysts under 300 W Xe-lamp (80 h irradiation) (adapted with permission from Wu et al. [117], copyright 2019, Wiley-VCH Verlag GmbH & Co. KGaA, Weinheim).

an EA/DI system where water served as the electron source, primarily produced CO for both the Fe-free components, PCN-221, and $MAPbI_3$@PCN-221. The high photocatalytic electron transfer rate is attributed to the strong interaction between $MAPbI_3$ QDs and the Fe catalytic sites within the MOF. The number of these catalytic sites plays a crucial role in the formation of CH_4. Furthermore, the high activity of the metal centers is linked to the porous and tunable crystal structure of the MOFs, which provides an excellent specific surface area for enhanced photocatalytic performance.

4.4 Organic-inorganic hybrid metal halide non-perovskite photocatalysts

Although inorganic organic hybrid perovskite systems show amazing application prospects, it is important to note that organic compounds with strong coordination abilities cover a wide range of categories. Therefore, using organic compounds as ligands has become a widely accepted strategy for synthesizing structurally novel catalysts without losing stability. Inorganic-organic hybrid non-perovskite compounds have emerged and demonstrated superior stability. For example, replacing MA^+ with hydrophobic quaternary ammonium cations, such as tetra-methyl ammonium [122,123] or tetra-butyl ammonium [124,125], which are adsorbed on the surface of as-prepared materials, has been reported to inhibit the absorption of water by the lattice. This modification enables photocatalysts to remain stable for over 30 days at a relative humidity of 90 ± 5% without any loss in photovoltaic performance [126]. In addition, the introduction of organic ligands often improves the energy level structure of all-inorganic materials, enhancing their light absorption capacity and adsorption of CO_2, making them more suitable for photocatalytic CO_2RR.

In 2022, Wu et al. [127] prepared brown plate-like monoclinic crystals, TMOF-10-NH_2(Br/I), using PbI_2 or $PbBr_2$ and 2-aminoterephthalic acid as the ligand via a hydrothermal method. This approach achieved a high yield of approximately 80% and excellent phase purity. The following discussion will focus on TMOF-10-NH_2 (I) for further analysis. Single crystal analysis revealed that, unlike the $FAPbBr_3$ perovskite mentioned earlier, TMOF-10-NH_2 exhibits an equal-network 3D coordination framework with 1D pores (Fig. 10(a)). The halogen-bridged, rod-like secondary structural units are formed by the planar inorganic components, extending along the *a*-axis in a sawtooth-like shape. Structurally, non-perovskite catalysts like TMOF-10-NH_2 differ significantly from the perovskite materials described earlier. The thermostability of TMOF-10-NH_2 can be maintained up to 200 °C, and it also shows high moisture stability in the range of 50% to 90% relative humidity (RH). Furthermore, even after 48 h of continuous illumination (300 W Xe lamp, 24 W/cm^2), its strong photostability remains intact. Stability tests, along with calculations of CO_2 and water vapor uptake in the material's pores, confirmed that TMOF-10-NH_2 provides a robust catalytic platform for photocatalytic CO_2RR in the presence of water vapor. DFT calculations indicate a lower CO_2 adsorption energy E_{Ads} of − 0.63 eV on the surface of

TMOF-10-NH_2, which is favorable compared to most reported photocatalysts [107]. This suggests that TMOF-10-NH_2 has superior CO_2 adsorption activity, which may be attributed to the strong interaction induced between oxygen atoms in $*CO_2$ and Pb^{2+} in TMOF-10-NH_2. The band structure plays a crucial role in enabling photocatalytic reactions. Valence band X-ray photoelectron spectroscopy (VB-XPS) revealed that the energy level of the valence band maximum (VBM) of TMOF-10-NH_2(I) is 1.78 eV, while the conduction band minimum (CBM) was estimated to be −1.11 eV based on Mott-Schottky analysis. Therefore, the CBM of TMOF-10-NH_2 is more negative than the redox potential of CO_2/CO (−0.48 V versus NHE, pH = 7) or CO_2/CH_4, while the VBM is more favorable than the redox potentials of O_2/H_2O (+0.82 V versus NHE, pH = 7) or H_2O_2/H_2O (+1.35 V versus NHE, pH = 7) (Fig. 10(b)). These results provide thermodynamic support for the realization of CO_2 photoreduction and H_2O oxidation on TMOF-10-NH_2. Additionally, photophysical studies, including surface photovoltage (SPV), transient absorption spectroscopy (TA), and Hall effect measurements, confirm the high carrier mobility and long carrier diffusion length in TMOF-10-NH_2.

The outstanding photocatalytic performance of TMOF-10-NH_2 is demonstrated in several tests. Under AM 1.5G simulated sunlight for 4 h, TMOF-10-NH_2 consistently emitted CO at an average rate of 78 μmol/(h·g), outperforming the majority of MOFs in CO_2 photoreduction by water vapor. In a continuous cycling experiment, TMOF-10-NH_2 successfully catalyzed the continuous production of CO for 24 h, showing little change in its structure (as confirmed by PXRD, FT-IR, and SEM characterization). These results validate the effective catalytic activity of TMOF-10-NH_2 in cyclic reactions and further highlight its high stability and excellent durability. The high CO release rate of TMOF-10-NH_2(I) indicates that its metal-iodine secondary building unit (SBUs) has better photocatalytic performance compared to conventional metal-oxo MOFs and other organolead halide materials (Fig. 10(c)) [128,129]. Notably, there is no direct contact between the aqueous medium and the photocatalyst, and the absence of Pb^{2+} leaching enhances the environmental friendliness

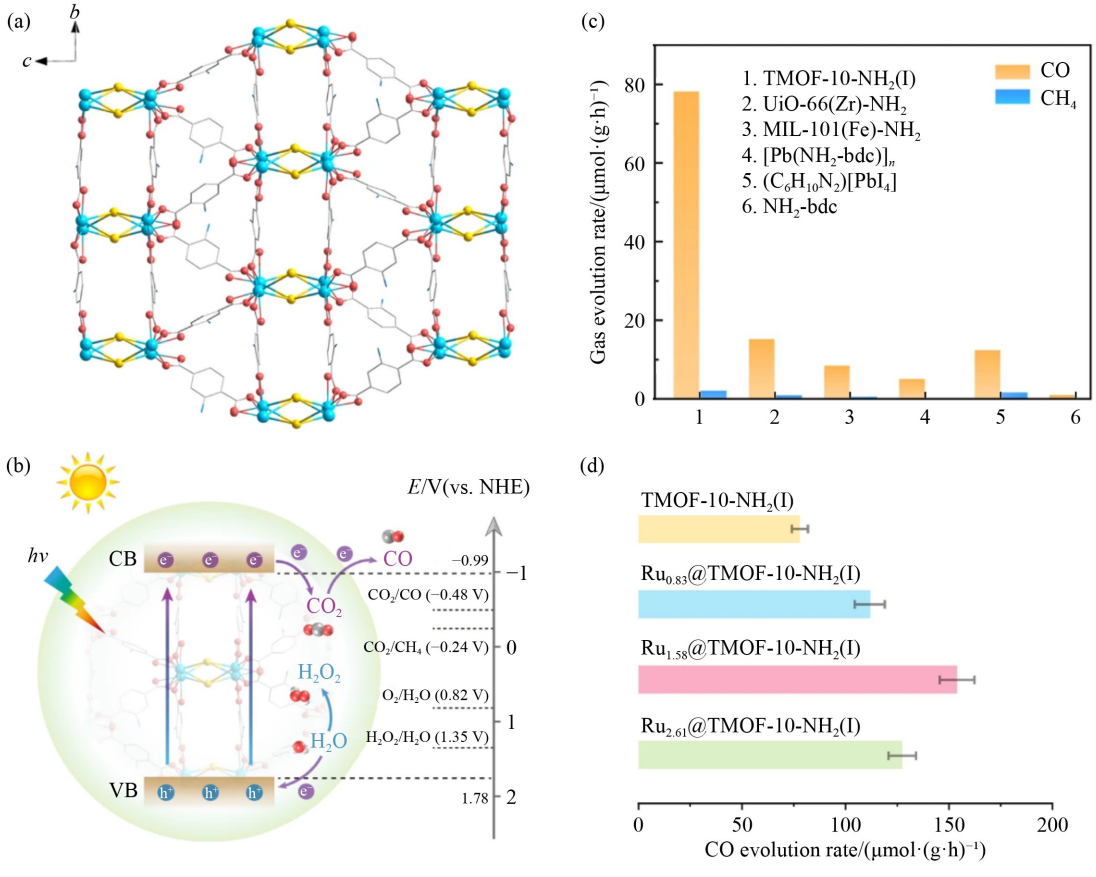

Fig. 10 A comprehensive analysis of the TMOF-10-NH_2 photocatalyst, encompassing micromolecular structure, band gap positioning, and product formation (adapted from Chen et al. [127] under the terms of CC BY license).

(a) Crystallographic view of TMOF-10-NH_2(I) along the a-axis; (b) schematic diagram of band structure of TMOF-10-NH_2(I); (c) comparison of CO release rates between TMOF-10-NH_2(I) and other MOFs; (d) CO evolution rate of TMOF-10-NH_2(I) with different Ru NPs loadings.

of these materials.

Intriguingly, when Ru nanoparticles (NPs) were successfully loaded onto the surface of TMOF-10-NH_2(I) crystals, the efficiency of photocatalytic CO_2RR was nearly doubled. The optimal loading amount was found to be 1.58% (mass fraction), as verified by inductively coupled plasma optical emission spectroscopy (ICP-OES). At this loading, the CO release rate reached 154 μmol/(g·h) (Fig. 10(d)), surpassing the vast majority of MOFs and/or lead halide hybrid catalysts, with no metal leaching or morphological changes observed. This enhancement can be attributed to the effective suppression of radiative electron-hole pair recombination in TMOF-10-NH_2(I) by the introduction of Ru NPs. Overall, this study provides valuable insights for the development of MOFs photocatalysts with halide-bridged SBUs, making small molecule activation and efficient photocarrier transport more promising in future research.

Building on this study, the photocatalysts TJU-31 and TJU-32 for the photocatalytic reduction of CO_2 to ethanol were reported several months later [45]. Both photocatalysts were synthesized using lead iodide as the precursor, with TJU-31 employing glutarate as the ligand and TJU-32 using iminodiacetate as the ligand (Fig. 11(a)). By precisely controlling the feeding ratio and reaction conditions, yellow plate-like and block-shaped crystals were obtained for TJU-31 and TJU-32, respectively. The phase purity of both materials was confirmed by the excellent agreement between their PXRD patterns and the simulated single-crystal data. Both TJU-31 and TJU-32 demonstrated excellent thermal stability, structural robustness and high photostability. This was confirmed by the absence of structural collapse after 24 h of continuous illumination at 270 °C, exposure to a wide pH range (4 to 10), boiling water conditions, and 90% RH. This stability is attributed to the formation of coordination grids, which contrasts with the ion binding nature of organolead iodide perovskites that are easily displaced by proton molecules [130]. Notably, in TJU-32, the –NH sites provided by-the ligands coordinate with additional Pb^{2+} centers, linking adjacent organic layers into a 3D sublattice. This transition from a two-dimensional (2D) to a three-dimensional (3D) structure creates asymmetric multi-metal sites, significantly reducing the energy barrier for C–C coupling during photocatalytic CO_2 reduction. As a result, this structure facilitates the efficient generation of C_2 product, particularly ethanol.

Ultraviolet photoelectron spectroscopy (UPS) and UV-vis data indicate that TJU-32 has a wide bandgap, with the VBM determined to be 1.98 V and the CBM at −0.64 V (Fig. 11(b)). Therefore, simultaneous CO_2 photoreduction and H_2O photooxidation are thermodynamically feasible.

After AM 1.5G simulated sunlight irradiation, TJU-32 not only steadily evolved ethanol at a rate of 17.6 μmol/(h·g), but also released CO and CH_4 at rates of 3.9 and 0.4 μmol/(h·g), respectively. The deposition of metal NPs as cocatalysts is a common strategy to enhance charge separation and photocatalytic activity. Similarly, loading various concentrations of Rh onto the crystal surface of TJU-32 using $RhCl_3$ solutions significantly enhanced charge separation and photocatalytic activity. Among the tested samples, $Rh_{0.11}$@TJU-32 showed the

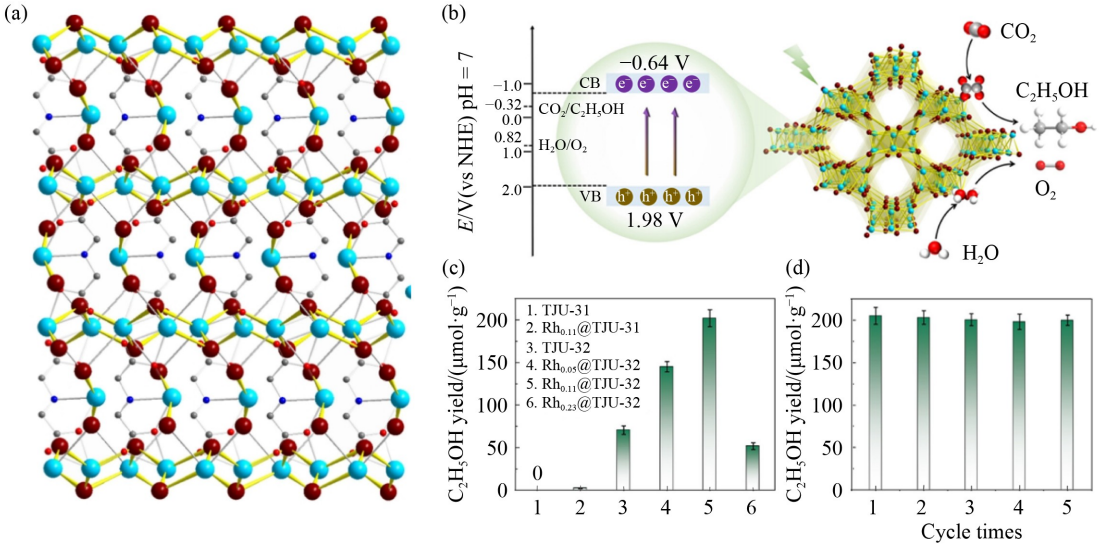

Fig. 11 Characterization and performance evaluation of TJU-32 (adapted with permission from Yin et al. [45], copyright 2024, Wiley-VCH GmbH).

(a) Complete crystallographic structure of TJU-32 along the *b*-axis; (b) sketch map of bandgap and photo-reduced CO_2 products of TJU-32; (c) yield of C_2H_5OH by photocatalysts loaded with different cocatalysts; (d) $Rh_{0.11}$@TJU-32 experimental results of catalyzing CO_2 to generate C_2H_5OH through five cycles.

highest ethanol evolution rate of 50.5 μmol/(h·g), which is three times higher than that of the parent TJU-32 (Fig. 11(c)). The corresponding selectivity for ethanol also increased from 80.4% to 89.4%, making it one of the highest among the developed CO_2 to C_2H_5OH photocatalysts reported to date. Notably, the results of five consecutive experiments showed no remarkable decrease in ethanol production (Fig. 11(d)), confirming the long-term photostability of $Rh_{0.11}$@TJU-32 under continuous irradiation for 20 h.

Several low-toxic or non-toxic metal cations have been reported as potential B-site components, exhibiting similar electronic structures and ionic radii to Pb^{2+}, thus showing promise as replacements. Recently, coordination polymers containing Cu^+ have become a hot topic in photocatalysis research. Bai and colleagues successfully used a dark red octahedral crystal, named NJU-Bai61 (Fig. 12(a)), to produce CH_4 through the photoreduction of CO_2 [131]. This study marks the first-time application of the $Cu(I)_xX_yL_z$ (X = Cl, Br, or I; L = organic ligands containing N, P, or S) coordination polymer for photocatalytic CO_2 reduction. In this system, Cu_4I_4 clusters adsorb photogenerated electrons and transfer them to $Cu_3OI(CO_2)_3$ clusters, which act as active sites for CO_2 adsorption and reduction. Theoretical calculations show that this process provides enough electrons for the reduction of CO_2 to CH_4. Experimental data indicate that after 4 h of illumination, NJU-Bai61 efficiently generates CH_4 with a yield of 15.75 μmol/(h·g) (Fig. 12(b)), exhibiting a high selectivity of 72.8% in aqueous solution, with only small amounts of CO and H_2 as by-products. Cyclic experiments showed no significant change in CH_4 generation activity (Fig. 12(c)), and XRD characterization confirmed that the crystal maintains robust stability before and after the photocatalytic reaction. This research provides significant insights into the development of lead-free catalysts for CO_2 photoreduction and the potential of new MOF systems.

The incorporation of metal ions into catalysts derived from certain MOF materials is considered an effective strategy for CO_2 photoreduction applications. Fei et al. successfully integrated a manganese halide complex into highly robust MOFs, using DMF/TEOA as a medium, and employed visible light to reduce CO_2 to formats

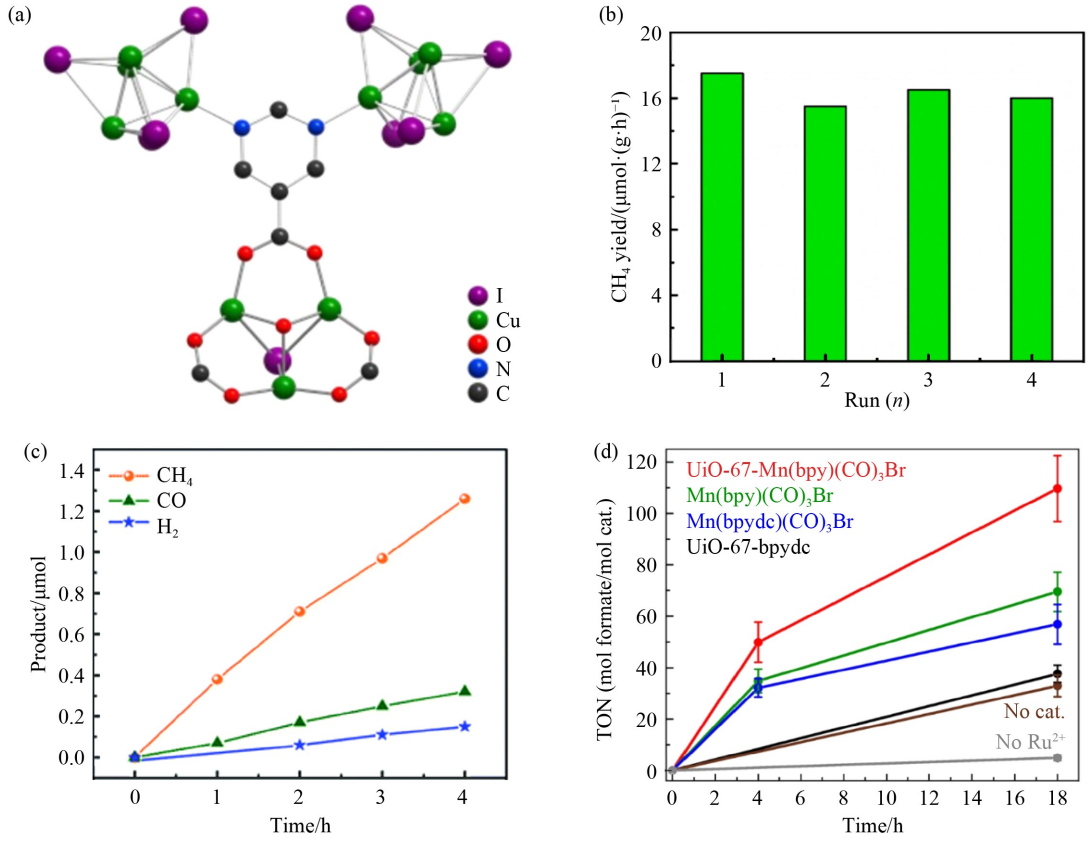

Fig. 12 Two types of organic-inorganic hybrid lead-free photocatalysts utilized in the domain of photoreduction of CO_2.

(a) Coordination environment of inorganic clusters and organic ligand pyrimidine-5-carboxylic acid (Hpmc) in NJU-Bai61; (b) yield of photocatalytic products varies with irradiation time over NJU-Bai61; (c) amount of CH_4 generated in four photocatalytic reactions, with NJU-Bai61 serving as the catalyst in each iteration ((a)–(c) adapted from Cao et al. [131] under the terms of CC BY 3.0 license); (d) graph depicting the formate turnover of the red sample UiO-67-Mn(bpy)$(CO)_3$Br, along with other materials, during a photocatalytic reaction (adapted with permission from Fei et al. [132], copyright 2015, American Chemical Society).

[132], a class of high-value products used as preservatives and antibacterial agents in livestock feed, as well as in the leather and textile industries. The turnover number of UiO-67-Mn(bpy)$(CO)_3$Br reached approximately 50 after 4 h of visible light irradiation at 470 nm, with 96% selectivity. Extended reaction times of up to 18 h resulted in a turnover number of about 110 (Fig. 12(d)), surpassing many noble metal-containing MOF catalysts. However, it is important to note that the lifespan of the prepared material cannot be solely defined by this turnover value, despite the photocatalytic reaction time being 18 h in the figure. The significant activity enhancement can be attributed to the sufficiently large pores of UiO-67, which facilitate electron transfer between Ru(II) photosensitizers and Mn complexes within the MOF. The framework backbone provides active sites for electron separation, improving the overall stability of the catalyst while preventing the dimerization of the Mn complex.

The aforementioned organic-inorganic hybrid metal halide materials offer a new reference point for coordination chemistry, providing a foundation for researchers to rationally design highly efficient materials for CO_2 photoreduction.

5 Summarization and prospectives

Photocatalysts for solar energy conversion and storage have garnered extensive research interest in recent years. Among these, metal halides have shown great development potential due to their excellent properties, sparking in-depth studies. This review introduces the common methods for synthesizing photocatalysts based on the fundamental mechanisms of photocatalytic CO_2 reduction, with a particular focus on hydrothermal synthesis, hot-injection, LARP, and anti-solvent precipitation. Moreover, it presents the latest progress in CO_2RR photocatalysts and exciting research in solar energy-driven applications, focusing on two main directions: organic-inorganic hybridization and all-inorganic systems, with perovskite and non-perovskite materials as subcategories. Table 2 summarizes some of the materials reported for photocatalytic CO_2RR in recent years.

In addition, various strategies to enhance photocatalytic performance are explored, including surface engineering (e.g., supported cocatalysts), tuning reaction parameters (e.g., solvent types, nanocrystal size), heterojunction engineering (e.g., integrating photocatalysts with MOFs), and composite engineering (e.g., halogen replacement, energy band adjustment, cation or anion regulation). While photocatalysts have made notable breakthroughs in this field, their widespread application is still in the early stages. To develop more efficient and compliant photocatalysts, several critical challenges must be addressed:

(1) Toxicity of Pb-based materials: For a long time, the superior performance of Pb-based photocatalytic materials has made them the most extensively studied. However, the high toxicity of Pb to both the environment and organisms remains the primary factor limiting their large-scale application [133]. Lead can leach from perovskites into plants, entering the human food chain [134], posing a serious threat to human health [135]. Therefore, the primary consideration for the long-term utilization of metal halide photocatalysts is replacing Pb at the B sites [11,136–138]. Several low- or non-toxic metal ions, such

Table 2 A summary of the photocatalytic performance of various metal halide catalysts in reducing CO_2

Photocatalysts	Reaction condition	Products	Yield	Ref.
$CsPbBr_3$ QDs	EA/H_2O	CO/CH_4	23.7 mmol/(g·h)	Xu et al. [88]
$CsPbBr_3$ QDs-Ni(bpy)	EA/H_2O	CO/CH_4	1252 μmol/(g·h)	Chen et al. [93]
$Rb_3Bi_2I_9$	H_2O vapor	CO/CH_4	CO: 18.2 μmol/g CH_4: 17.0 μmol/g	Bhosale et al. [94]
$Cs_3Bi_2I_9$	H_2O vapor	CO/CH_4	CO: 77.6 μmol/g CH_4: 14.9 μmol/g	Bhosale et al. [94]
$Cs_3Sb_2Br_9$	H_2O	CO	103.3 μmol/(g·h)	Lu et al. [95]
$Cs_2AgBiBr_6$	EA	CO/CH_4	CO: 14.1 μmol/g CH_4: 9.6 μmol/g	Zhou et al. [96]
Bi_5O_7I	Gas-solid/H_2O	CO	10.67 μmol/g	Wang et al. [103]
PML-Cu/$Bi_{12}O_{17}Br_2$	H_2O	CO	116.86 μmol/(g·h)	Zhang et al. [105]
OV-Bi-rich $Bi_{12}O_{17}Cl_2$	Liquid-solid/H_2O	CO	64 μmol/(g·h)	Guan et al. [110]
2Co-BiOCl	Gas-solid/H_2O	CO	183.9 μmol/(g·h)	Zhao et al. [111]
$FAPbBr_3$ QDs	EA/DI	CO	181.25 μmol/(g·h)	Que et al. [119]
$MA_3Bi_2I_9$	H_2O vapor	CO/CH_4	CO: 10.4 μmol/g CH_4: 7.2 μmol/g	Bhosale et al. [94]
Ru@TMOF-10-NH_2	H_2O vapor	CO	154 μmol/(g·h)	Chen et al. [127]
$Rh_{0.11}$@TJU-32	H_2O vapor	C_2H_5OH	50.5 μmol/(g·h)	Yin et al. [45]
NJU-Bai61	H_2O/TEA	CH_4	15.75 μmol/(g·h)	Gao et al. [131]
UiO-67-Mn(bpy)$(CO)_3$Br	DMF/TEOA	Formate	TON = 50 (4 h); 110 (18 h)	Fei et al. [132]

as Bi^{3+}, Cu^{+}, Sn^{2+}, and Ag^{+}, have been explored as potential substitutes for lead. These lead-free environmentally friendly photocatalysts not only eliminate Pb-related toxicity, but also exhibit higher catalytic activity and chemical stability [139–143]. Nevertheless, their performance still lags behind that of Pb-based materials, highlighting a significant opportunity for improvement in the development of efficient lead-free photocatalysts.

(2) Stability under harsh conditions: Metal halide catalysts often struggle to maintain structural stability under high temperature, humidity, and light conditions, primarily due to the more active chemical bonds at the particle surface and weaker interactions between ligands and metals. Additionally, the ionic bonding nature of metal halide materials makes them more prone to decomposition. To improve catalyst stability, it is essential to use organic ligands that bind more firmly to metal atoms during synthesis or to create protective passivation layers on the material's surface. For example, encapsulating material molecules within a waterproof framework can help ensure long-term stability while maintaining or even enhancing catalytic performance [117].

(3) Production of high-value hydrocarbon products: To date, the majority of metal halide photocatalysts have thus far been limited to reducing CO_2 to C_1 products, such as CO, or HCOOH, through the two-electron ($2e^-$) reduction process. The ability to synthesize more advanced hydrocarbon energy products containing multiple carbon atoms through $4e^-$, $6e^-$, or $8e^-$ reduction remains a long-awaited goal. This highlights the importance of gaining a deeper understanding of the reaction mechanisms in photocatalytic CO_2 reduction to produce high-value organic compounds.

In summary, metal halides hold great potential for solar energy conversion to green energy. Further research and development of robust metal halide photocatalytic materials are essential to advancing solar-driven technologies and achieving a low-carbon future. It is hoped that this review provides valuable insights into recent advancements in photocatalysis, contributing significantly to the scientific research and application of the photovoltaic industry.

Acknowledgements This work was supported by the National Natural Science Foundation of China (Grant Nos. 22201220 and 52172152) and the National Natural Science Foundation of Zhejiang Province, China (Grant No. LQ22B010003).

Competing Interests The authors declare that they have no competing interests.

References

1. Wang J, Liu J L, Du Z L, et al. Recent advances in metal halide perovskite photocatalysts: Properties, synthesis and applications. Journal of Energy Chemistry, 2021, 54: 770–785
2. Wang G Q, Zhang F J, Wang Y R, et al. Research progress on photocatalytic reduction of CO_2 based on $CsPbBr_3$ perovskite materials. ChemNanoMat: Chemistry of Nanomaterials for Energy, Biology and More, 2022, 8(8): e202200230
3. Collado L, Reynal A, Fresno F, et al. Unravelling the effect of charge dynamics at the plasmonic metal/semiconductor interface for CO_2 photoreduction. Nature Communications, 2018, 9(1): 4986
4. Roy S C, Varghese O K, Paulose M, et al. Toward solar fuels: Photocatalytic conversion of carbon dioxide to hydrocarbons. ACS Nano, 2010, 4(3): 1259–1278
5. Zhou J, Chen W C, Sun C Y, et al. Oxidative polyoxometalates modified graphitic carbon nitride for visible-light CO_2 reduction. ACS Applied Materials & Interfaces, 2017, 9(13): 11689–11695
6. Tu W G, Zhou Y, Zou Z G. Photocatalytic conversion of CO_2 into renewable hydrocarbon fuels: State-of-the-art accomplishment, challenges, and prospects. Advanced Materials, 2014, 26(27): 4607–4626
7. Habisreutinger S N, Schmidt-Mende L, Stolarczyk J K. Photocatalytic reduction of CO_2 on TiO_2 and other semiconductors. Angewandte Chemie International Edition, 2013, 52(29): 7372–7408
8. Du Z L, Artemyev M, Wang J, et al. Performance improvement strategies for quantum dot-sensitized solar cells: A review. Journal of Materials Chemistry. A, Materials for Energy and Sustainability, 2019, 7(6): 2464–2489
9. Wang D H, Yin F F, Du Z L, et al. Recent progress in quantum dot-sensitized solar cells employing metal chalcogenides. Journal of Materials Chemistry. A, Materials for Energy and Sustainability, 2019, 7(46): 26205–26226
10. Dong W J, Ji Y M, Wang J, et al. Evolution of the properties and composition of heavy oil by injecting dry boiler flue gas. ACS Omega, 2021, 6(50): 34675–34686
11. Hiragond C B, Powar N S, In S I. Recent developments in lead and lead-free halide perovskite nanostructures towards photocatalytic CO_2 reduction. Nanomaterials, 2020, 10(12): 2569
12. Li X, Yu J G, Jaroniec M, et al. Cocatalysts for selective photoreduction of CO_2 into solar fuels. Chemical Reviews, 2019, 119(6): 3962–4179
13. Sorcar S, Hwang Y J, Lee J W, et al. CO_2, water, and sunlight to hydrocarbon fuels: A sustained sunlight to fuel (Joule-to-Joule) photoconversion efficiency of 1%. Energy & Environmental Science, 2019, 12(9): 2685–2696
14. Ali S, Flores M C, Razzaq A, et al. Gas phase photocatalytic CO_2 reduction, "A brief overview for benchmarking". Catalysts, 2019, 9(9): 727
15. Hiragond C, Ali S, Sorcar S, et al. Hierarchical nanostructured photocatalysts for CO_2 photoreduction. Catalysts, 2019, 9(4): 370
16. Ali S, Lee J, Kim H, et al. Sustained, photocatalytic CO_2 reduction to CH_4 in a continuous flow reactor by earth-abundant materials: Reduced titania-Cu_2O Z-scheme heterostructures. Applied Catalysis B: Environmental, 2020, 279: 119344
17. Chen X B, Shen S H, Guo L J, et al. Semiconductor-based photocatalytic hydrogen generation. Chemical Reviews, 2010,

110(11): 6503–6570
18. Singh A K, Montoya J H, Gregoire J M, et al. Robust and synthesizable photocatalysts for CO_2 reduction: A data-driven materials discovery. Nature Communications, 2019, 10(1): 443
19. Ran J R, Jaroniec M, Qiao S Z. Cocatalysts in semiconductor-based photocatalytic CO_2 reduction: Achievements, challenges, and opportunities. Advanced Materials, 2018, 30(7): 1704649
20. Schreier M, Héroguel F, Steier L, et al. Solar conversion of CO_2 to CO using earth-abundant electrocatalysts prepared by atomic layer modification of CuO. Nature Energy, 2017, 2(7): 17087
21. Zhu X L, Lin Y X, San Martin J, et al. Lead halide perovskites for photocatalytic organic synthesis. Nature Communications, 2019, 10(1): 2843
22. Ketavath R, Mohan L, Sumukam R R, et al. Can perovskites be efficient photocatalysts in organic transformations? Journal of Materials Chemistry. A, Materials for Energy and Sustainability, 2022, 10(23): 12317–12333
23. Wang J, Xia T, Wang L, et al. Enabling visible-light-driven selective CO_2 reduction by doping quantum dots: Trapping electrons and suppressing H_2 evolution. Angewandte Chemie International Edition, 2018, 57(50): 16447–16451
24. Cui X F, Wang J, Liu B, et al. Turning Au nanoclusters catalytically active for visible-light-driven CO_2 reduction through bridging ligands. Journal of the American Chemical Society, 2018, 140(48): 16514–16520
25. Li H J, Zhou Y, Tu W G, et al. State-of-the-art progress in diverse heterostructured photocatalysts toward promoting photocatalytic performance. Advanced Functional Materials, 2015, 25(7): 998–1013
26. Wang Q, Domen K. Particulate photocatalysts for light-driven water splitting: Mechanisms, challenges, and design strategies. Chemical Reviews, 2020, 120(2): 919–985
27. Wu H L, Li X B, Tung C H, et al. Semiconductor quantum dots: An emerging candidate for CO_2 photoreduction. Advanced Materials, 2019, 31(36): 1900709
28. Xie S J, Zhang Q H, Liu G D, et al. Photocatalytic and photoelectrocatalytic reduction of CO_2 using heterogeneous catalysts with controlled nanostructures. Chemical Communications, 2016, 52(1): 35–59
29. DuBose J T, Kamat P V. Efficacy of perovskite photocatalysis: Challenges to overcome. ACS Energy Letters, 2022, 7(6): 1994–2011
30. Li K, Peng B S, Peng T Y. Recent advances in heterogeneous photocatalytic CO_2 conversion to solar fuels. ACS Catalysis, 2016, 6(11): 7485–7527
31. Zhang L, Miao J H, Li J F, et al. Halide perovskite materials for energy storage applications. Advanced Functional Materials, 2020, 30(40): 2003653
32. Chen P F, Ong W J, Shi Z H, et al. Pb-based halide perovskites: Recent advances in photo(electro)catalytic applications and looking beyond. Advanced Functional Materials, 2020, 30(30): 1909667
33. Huang H W, Pradhan B, Hofkens J, et al. Solar-driven metal halide perovskite photocatalysis: Design, stability, and performance. ACS Energy Letters, 2020, 5(4): 1107–1123
34. Han C, Zhu X L, Martin J S, et al. Recent progress in engineering metal halide perovskites for efficient visible-light-driven photocatalysis. ChemSusChem, 2020, 13(16): 4005–4025
35. Ma S Q, Chen D M, Zhong Y, et al. Oxygen vacancy simultaneously inducing peroxymonosulfate activation and photocatalytic reaction for highly efficient ciprofloxacin degradation. Chemical Engineering Journal, 2023, 467: 143385
36. Purohit S, Yadav K L, Satapathi S. Metal halide perovskite heterojunction for photocatalytic hydrogen generation: Progress and future opportunities. Advanced Materials Interfaces, 2022, 9(15): 2200058
37. Das R, Patra A, Dutta S K, et al. Facets-directed epitaxially grown lead halide perovskite-sulfobromide nanocrystal heterostructures and their improved photocatalytic activity. Journal of the American Chemical Society, 2022, 144(40): 18629–18641
38. Li X X, Zheng S T. Three-dimensional metal-halide open frameworks. Coordination Chemistry Reviews, 2021, 430: 213663
39. Kumar A, Krishnan V. Vacancy engineering in semiconductor photocatalysts: Implications in hydrogen evolution and nitrogen fixation applications. Advanced Functional Materials, 2021, 31(28): 2009807
40. Shi E Z, Gao Y, Finkenauer B P, et al. Two-dimensional halide perovskite nanomaterials and heterostructures. Chemical Society Reviews, 2018, 47(16): 6046–6072
41. Pang H R, Du S J, Deng J P, et al. Enhancing carrier transport in 2D/3D perovskite heterostructures through organic cation fluorination. Small, 2024, 20(34): 2401797
42. San Martin J, Dang N, Raulerson E, et al. Perovskite photocatalytic CO_2 reduction or photoredox organic transformation? Angewandte Chemie International Edition, 2022, 61(39): e202205572
43. Liu G N, Gao C C, Qi F Z, et al. Band edge modulation via a hydrogen-bond-free cation in hybrid bismuth iodine for overall photocatalytic CO_2 reduction. Inorganic Chemistry Frontiers, 2024, 11(14): 4364–4373
44. Fang S Y, Rahaman M, Bharti J, et al. Photocatalytic CO_2 reduction. Nature Reviews. Methods Primers, 2023, 3(1): 61
45. Yin J L, Song X L, Chen S, et al. Modulating inorganic dimensionality of ultrastable lead halide coordination polymers for photocatalytic CO_2 reduction to ethanol. Angewandte Chemie International Edition, 2024, 63(16): e202316080
46. Walter M G, Warren E L, McKone J R, et al. Solar water splitting cells. Chemical Reviews, 2010, 110(11): 6446–6473
47. Zou H Y, Dong C W, Li S Y, et al. Effect of surface trap states on photocatalytic activity of semiconductor quantum dots. Journal of Physical Chemistry C, 2018, 122(17): 9312–9319
48. Huang H, Bodnarchuk M I, Kershaw S V, et al. Lead halide perovskite nanocrystals in the research spotlight: Stability and defect tolerance. ACS Energy Letters, 2017, 2(9): 2071–2083
49. Kovalenko M V, Protesescu L, Bodnarchuk M I. Properties and potential optoelectronic applications of lead halide perovskite nanocrystals. Science, 2017, 358(6364): 745–750
50. Brandt R E, Poindexter J R, Gorai P, et al. Searching for "Defect-Tolerant" photovoltaic materials: Combined theoretical and experimental screening. Chemistry of Materials, 2017,

29(11): 4667–4674
51. Zhong F Y, He Y, Sun Y J, et al. Metal-doping of halide perovskite nanocrystals for energy and environmental photocatalysis: Challenges and prospects. Journal of Materials Chemistry A, 2022, 10(43): 22915–22928
52. Pi J C, Jia X F, Long Z W, et al. Surface and defect engineering coupling of halide double perovskite $Cs_2NaBiCl_6$ for efficient CO_2 photoreduction. Advanced Energy Materials, 2022, 12(43): 2202074
53. Min H, Lee D Y, Kim J, et al. Perovskite solar cells with atomically coherent interlayers on SnO_2 electrodes. Nature, 2021, 598(7881): 444–450
54. Kim D, Jung H J, Park I J, et al. Efficient, stable silicon tandem cells enabled by anion-engineered wide-bandgap perovskites. Science, 2020, 368(6487): 155–160
55. Zhang G, Liu G, Wang L Z, et al. Inorganic perovskite photocatalysts for solar energy utilization. Chemical Society Reviews, 2016, 45(21): 5951–5984
56. Wu D F, Zhao X S, Huang Y Y, et al. Lead-free perovskite Cs_2AgBiX_6 nanocrystals with a band gap funnel structure for photocatalytic CO_2 reduction under visible light. Chemistry of Materials, 2021, 33(13): 4971–4976
57. Spanopoulos I, Hadar I, Ke W J, et al. Water-stable 1D hybrid tin(II) iodide emits broad light with 36% photoluminescence quantum efficiency. Journal of the American Chemical Society, 2020, 142(19): 9028–9038
58. Zhang H F, Yang Z, Yu W, et al. A sandwich-like organolead halide perovskite photocathode for efficient and durable photoelectrochemical hydrogen evolution in water. Advanced Energy Materials, 2018, 8(22): 1800795
59. Simenas M, Balciunas S, Wilson J N, et al. Suppression of phase transitions and glass phase signatures in mixed cation halide perovskites. Nature Communications, 2020, 11(1): 5103
60. Shamsi J, Urban A S, Imran M, et al. Metal halide perovskite nanocrystals: synthesis, post-synthesis modifications, and their optical properties. Chemical Reviews, 2019, 119(5): 3296–3348
61. Yin J L, Li D Y, Sun C, et al. Solar-driven conversion of CO_2 to C_2 products by the 3d transition metal intercalates of layered lead iodides. Advanced Materials, 2024, 36(30): 2403651
62. Wang C, Xiao J W, Yan Z G, et al. Colloidal synthesis and phase transformation of all-inorganic bismuth halide perovskite nanoplates. Nano Research, 2023, 16(1): 1703–1711
63. Kovalenko M V, Manna L, Cabot A, et al. Prospects of nanoscience with nanocrystals. ACS Nano, 2015, 9(2): 1012–1057
64. Zhang C X, Chen J Y, Wang S, et al. Metal halide perovskite nanorods: shape matters. Advanced Materials, 2020, 32(46): 2002736
65. Rao M K, Selvakumar M, Mahesha M G, et al. Tackling toxicity and stability using eco-friendly metal-halide ion substituted perovskite nanocrystals for advanced display color conversion. Chemical Engineering Journal, 2024, 494: 152918
66. Chen Z Y, Dhakal T P. Room temperature synthesis of lead-free $FASnI_3$ perovskite nanocrystals with improved stability by SnF_2 additive. Applied Physics Reviews, 2023, 10(1): 011404
67. Protesescu L, Yakunin S, Bodnarchuk M I, et al. Nanocrystals of cesium lead halide perovskites ($CsPbX_3$, X = Cl, Br, and I): novel optoelectronic materials showing bright emission with wide color gamut. Nano Letters, 2015, 15(6): 3692–3696
68. Wong A B, Bekenstein Y, Kang J, et al. Strongly quantum confined colloidal cesium tin iodide perovskite nanoplates: Lessons for reducing defect density and improving stability. Nano Letters, 2018, 18(3): 2060–2066
69. Shamsi J, Rastogi P, Caligiuri V, et al. Bright-emitting perovskite films by large-scale synthesis and photoinduced solid-state transformation of $CsPbBr_3$ nanoplatelets. ACS Nano, 2017, 11(10): 10206–10213
70. Wei S, Yang Y C, Kang X J, et al. Room - temperature and gram-scale synthesis of $CsPbX_3$ (X = Cl, Br, I) perovskite nanocrystals with 50–85% photoluminescence quantum yields. Chemical Communications, 2016, 52(45): 7265–7268
71. Wang K H, Wu L, Li L, et al. Large-scale synthesis of highly luminescent perovskite-related $CsPb_2Br_5$ nanoplatelets and their fast anion exchange. Angewandte Chemie International Edition, 2016, 55(29): 8328–8332
72. Feng Y M, Chen D M, Niu M, et al. Recent progress in metal halide perovskite-based photocatalysts: Physicochemical properties, synthetic strategies, and solar-driven applications. Journal of Materials Chemistry A, 2023, 11(41): 22058–22086
73. Xiao M D, Huang F Z, Huang W C, et al. A fast deposition-crystallization procedure for highly efficient lead iodide perovskite thin-film solar cells. Angewandte Chemie International Edition, 2014, 53(37): 9898–9903
74. Jeon N J, Noh J H, Kim Y C, et al. Solvent engineering for high-performance inorganic–organic hybrid perovskite solar cells. Nature Materials, 2014, 13(9): 897–903
75. Petrus M L, Schlipf J, Li C, et al. Capturing the sun: a review of the challenges and perspectives of perovskite solar cells. Advanced Energy Materials, 2017, 7(16): 1700264
76. Huang H W, Yuan H F, Janssen K P F, et al. Efficient and selective photocatalytic oxidation of benzylic alcohols with hybrid organic–inorganic perovskite materials. ACS Energy Letters, 2018, 3(4): 755–759
77. Wu D F, Zhou J E, Kang W, et al. Ultrastable lead-free $CsAgCl_2$ perovskite microcrystals for photocatalytic CO_2 reduction. Journal of Physical Chemistry Letters, 2021, 12(21): 5110–5114
78. Wu Y Q, Wang P, Zhu X L, et al. Composite of $CH_3NH_3PbI_3$ with reduced graphene oxide as a highly efficient and stable visible-light photocatalyst for hydrogen evolution in aqueous HI solution. Advanced Materials, 2018, 30(7): 1704342
79. Zhao H B, Liao J F, Teng Y, et al. Inorganic copper-based halide perovskite for efficient photocatalytic CO_2 reduction. ACS Applied Materials & Interfaces, 2022, 14(38): 43354–43361
80. Wu D F, Wang C, Huo B J, et al. Photo- and electrocatalytic CO_2 reduction based on stable lead-free perovskite Cs_2PdBr_6. Energy & Environmental Materials, 2023, 6(5): e12411
81. Wang J, Shi Y Y, Wang Y H, et al. Rational design of metal halide perovskite nanocrystals for photocatalytic CO_2 reduction: Recent advances, challenges, and prospects. ACS Energy Letters, 2022, 7(6): 2043–2059
82. Li Q L, Song T, Zhang Y P, et al. Boosting photocatalytic

activity and stability of lead-free $Cs_3Bi_2Br_9$ perovskite nanocrystals via *in situ* growth on monolayer 2D $Ti_3C_2T_x$ MXene for C–H bond oxidation. ACS Applied Materials & Interfaces, 2021, 13(23): 27323–27333

83. Zhang W N, Zhao Q G, Wang X H, et al. Lead-free organic–inorganic hybrid perovskite heterojunction composites for photocatalytic applications. Catalysis Science & Technology, 2017, 7(13): 2753–2762
84. Gao G, Xi Q Y, Zhou H, et al. Novel inorganic perovskite quantum dots for photocatalysis. Nanoscale, 2017, 9(33): 12032–12038
85. Cardenas-Morcoso D, Gualdrón-Reyes A F, Ferreira Vitoreti A B, et al. Photocatalytic and photoelectrochemical degradation of organic compounds with all-inorganic metal halide perovskite quantum dots. Journal of Physical Chemistry Letters, 2019, 10(3): 630–636
86. Chouhan A S, Jasti N P, Hadke S, et al. Large grained and high charge carrier lifetime $CH_3NH_3PbI_3$ thin-films:Implications for perovskite solar cells. Current Applied Physics, 2017, 17(10): 1335–1340
87. Zhang F Y, Yang B, Li Y J, et al. Extra long electron–hole diffusion lengths in $CH_3NH_3PbI_{3-x}Cl_x$ perovskite single crystals. Journal of Materials Chemistry C, 2017, 5(33): 8431–8435
88. Xu Y F, Yang M Z, Chen B X, et al. A $CsPbBr_3$ perovskite quantum dot/graphene oxide composite for photocatalytic CO_2 reduction. Journal of the American Chemical Society, 2017, 139(16): 5660–5663
89. Wei Y, Cheng Z Y, Lin J. An overview on enhancing the stability of lead halide perovskite quantum dots and their applications in phosphor-converted LEDs. Chemical Society Reviews, 2019, 48(1): 310–350
90. Park Y H, Murali G, Modigunta J K R, et al. Recent advances in quantum dots for photocatalytic CO_2 reduction: A mini-review. Frontiers in Chemistry, 2021, 9: 734108
91. Shyamal S, Pradhan N. Halide perovskite nanocrystal photocatalysts for CO_2 reduction: Successes and challenges. Journal of Physical Chemistry Letters, 2020, 11(16): 6921–6934
92. Hou J G, Cao S Y, Wu Y Z, et al. Inorganic colloidal perovskite quantum dots for robust solar CO_2 reduction. Chemistry – A European Journal, 2017, 23(40): 9481–9485
93. Chen Z J, Hu Y G, Wang J, et al. Boosting photocatalytic CO_2 reduction on $CsPbBr_3$ perovskite nanocrystals by immobilizing metal complexes. Chemistry of Materials, 2020, 32(4): 1517–1525
94. Bhosale S S, Kharade A K, Jokar E, et al. Mechanism of photocatalytic CO_2 reduction by bismuth-based perovskite nanocrystals at the gas–solid interface. Journal of the American Chemical Society, 2019, 141(51): 20434–20442
95. Lu C, Itanze D S, Aragon A G, et al. Synthesis of lead-free $Cs_3Sb_2Br_9$ perovskite alternative nanocrystals with enhanced photocatalytic CO_2 reduction activity. Nanoscale, 2020, 12(5): 2987–2991
96. Zhou L, Xu Y F, Chen B X, et al. Synthesis and photocatalytic application of stable lead-free $Cs_2AgBiBr_6$ perovskite nanocrystals. Small, 2018, 14(11): 1703762
97. Zhou C K, Lin H R, Lee S J, et al. Organic–inorganic metal halide hybrids beyond perovskites. Materials Research Letters, 2018, 6(10): 552–569
98. Connor B A, Leppert L, Smith M D, et al. Layered halide double perovskites: dimensional reduction of $Cs_2AgBiBr_6$. Journal of the American Chemical Society, 2018, 140(15): 5235–5240
99. Liu Z Y, Yang H J, Wang J Y, et al. Synthesis of lead-free Cs_2AgBiX_6 (X = Cl, Br, I) double perovskite nanoplatelets and their application in CO_2 photocatalytic reduction. Nano Letters, 2021, 21(4): 1620–1627
100. Zhao X G, Yang J H, Fu Y H, et al. Design of lead-free inorganic halide perovskites for solar cells via cation-transmutation. Journal of the American Chemical Society, 2017, 139(7): 2630–2638
101. Yan G, Sun X D, Zhang Y, et al. Metal-free 2D/2D van der Waals heterojunction based on covalent organic frameworks for highly efficient solar energy catalysis. Nano-Micro Letters, 2023, 15(1): 132
102. Zhang Y, Zhang G P, Di J, et al. Bismuth-based materials for CO_2 photoreduction. Current Opinion in Green and Sustainable Chemistry, 2023, 39: 100718
103. Wang Y X, Wang H, Sheng J P, et al. Self-templated fabrication of porous Bi_5O_7I nanosheets for enhanced visible light CO_2 photoreduction. Surfaces and Interfaces, 2023, 43: 103551
104. Li Q, Li Y L, Li B, et al. Construction of adjustable dominant {314} facet of Bi_5O_7I and facet-oxygen vacancy coupling dependent adsorption and photocatalytic activity. Applied Catalysis B: Environmental, 2021, 289: 120041
105. Zhang Y, Guo F Y, Di J, et al. Strain-induced surface interface dual polarization constructs PML-Cu/$Bi_{12}O_{17}Br_2$ high-density active sites for CO_2 photoreduction. Nano-Micro Letters, 2024, 16(1): 90
106. Han N, Zhang W, Guo W, et al. Designing oxide catalysts for oxygen electrocatalysis: Insights from mechanism to application. Nano-Micro Letters, 2023, 15(1): 185
107. Xu F Y, Meng K, Cheng B, et al. Unique S-scheme heterojunctions in self-assembled TiO_2/$CsPbBr_3$ hybrids for CO_2 photoreduction. Nature Communications, 2020, 11(1): 4613
108. Chen F, Huang H W, Guo L, et al. The role of polarization in photocatalysis. Angewandte Chemie International Edition, 2019, 58(30): 10061–10073
109. Di J, Jiang W, Liu Z. Symmetry breaking for semiconductor photocatalysis. Trends in Chemistry, 2022, 4(11): 1045–1055
110. Guan M L, Lu N, Zhang X, et al. Engineering of oxygen vacancy and bismuth cluster assisted ultrathin $Bi_{12}O_{17}Cl_2$ nanosheets with efficient and selective photoreduction of CO_2 to CO. Carbon Energy, 2024, 6(4): e420
111. Zhao L L, Hou H L, Wang S, et al. Engineering Co single atoms in ultrathin BiOCl nanosheets for boosted CO_2 photoreduction. Advanced Functional Materials, 2024, 2416346
112. Nedelcu G, Protesescu L, Yakunin S, et al. Fast anion-exchange in highly luminescent nanocrystals of cesium lead halide perovskites ($CsPbX_3$, X = Cl, Br, I). Nano Letters, 2015, 15(8): 5635–5640
113. Swarnkar A, Marshall A R, Sanehira E M, et al. Quantum dot–induced phase stabilization of α-$CsPbI_3$ perovskite for high-efficiency photovoltaics. Science, 2016, 354(6308): 92–95

114. Li X M, Yu D J, Cao F, et al. Healing all-inorganic perovskite films via recyclable dissolution–recyrstallization for compact and smooth carrier channels of optoelectronic devices with high stability. Advanced Functional Materials, 2016, 26(32): 5903–5912
115. Zhang X Y, Sun C, Zhang Y, et al. Bright perovskite nanocrystal films for efficient light-emitting devices. Journal of Physical Chemistry Letters, 2016, 7(22): 4602–4610
116. Yakunin S, Protesescu L, Krieg F, et al. Erratum: Low-threshold amplified spontaneous emission and lasing from colloidal nanocrystals of caesium lead halide perovskites. Nature Communications, 2015, 6(1): 8515
117. Wu L Y, Mu Y F, Guo X X, et al. Encapsulating perovskite quantum dots in iron-based metal–organic frameworks (MOFs) for efficient photocatalytic CO_2 reduction. Angewandte Chemie International Edition, 2019, 58(28): 9491–9495
118. Protesescu L, Yakunin S, Bodnarchuk M I, et al. Monodisperse formamidinium lead bromide nanocrystals with bright and stable green photoluminescence. Journal of the American Chemical Society, 2016, 138(43): 14202–14205
119. Que M D, Zhao Y, Pan L K, et al. Colloidal formamidinium lead bromide quantum dots for photocatalytic CO_2 reduction. Materials Letters, 2021, 282: 128695
120. McCall K M, Stoumpos C C, Kostina S S, et al. Strong electron–phonon coupling and self-trapped excitons in the defect halide perovskites $A_3M_2I_9$ (A = Cs, Rb; M=Bi, Sb). Chemistry of Materials, 2017, 29(9): 4129–4145
121. Xiao M, Zhang Y R, You J K, et al. Addressing the stability challenge of metal halide perovskite based photocatalysts for solar fuel production. Journal of Physics: Energy, 2022, 4(4): 042005
122. Du X Z, Qiu R Z, Zou T Y, et al. Enhanced uniformity and stability of Pb–Sn perovskite solar cells via Me_4NBr passivation. Advanced Materials Interfaces, 2019, 6(14): 1900413
123. Parida B, Jin I S, Jung J W. Dual passivation of SnO_2 by tetramethylammonium chloride for high-performance $CsPbI_2Br$ -based inorganic perovskite solar cells. Chemistry of Materials, 2021, 33(15): 5850–5858
124. Poli I, Eslava S, Cameron P. Tetrabutylammonium cations for moisture-resistant and semitransparent perovskite solar cells. Journal of Materials Chemistry. A, 2017, 5(42): 22325–22333
125. Xu Z Y, Chen R H, Wu Y Z, et al. Br-containing alkyl ammonium salt-enabled scalable fabrication of high-quality perovskite films for efficient and stable perovskite modules. Journal of Materials Chemistry. A, 2019, 7(47): 26849–26857
126. Zhao H, Kordas K, Ojala S. Recent advances in synthesis of water-stable metal halide perovskites and photocatalytic applications. Journal of Materials Chemistry. A, Materials for Energy and Sustainability, 2023, 11(42): 22656–22687
127. Chen X F, Peng C D, Dan W Y, et al. Bromo- and iodo-bridged building units in metal-organic frameworks for enhanced carrier transport and CO_2 photoreduction by water vapor. Nature Communications, 2022, 13(1): 4592
128. Sun D R, Fu Y H, Liu W J, et al. Studies on photocatalytic CO_2 reduction over NH_2-Uio-66(Zr) and its derivatives: towards a better understanding of photocatalysis on metal–organic frameworks. Chemistry – A European Journal, 2013, 19(42): 14279–14285
129. Dao X Y, Guo J H, Wei Y P, et al. Solvent-free photoreduction of CO_2 to CO catalyzed by Fe-MOFs with superior selectivity. Inorganic Chemistry, 2019, 58(13): 8517–8524
130. Song X L, Wei G F, Sun J, et al. Overall photocatalytic water splitting by an organolead iodide crystalline material. Nature Catalysis, 2020, 3(12): 1027–1033
131. Gao Y J, Zhang L, Gu Y M, et al. Formation of a mixed-valence Cu(i)/Cu(ii) metal–organic framework with the full light spectrum and high selectivity of CO_2 photoreduction into CH_4. Chemical Science, 2020, 11(37): 10143–10148
132. Fei H H, Sampson M D, Lee Y, et al. Photocatalytic CO_2 reduction to formate using a Mn(I) molecular catalyst in a robust metal–organic framework. Inorganic Chemistry, 2015, 54(14): 6821–6828
133. Bresolin B M, Park Y, Bahnemann D W. Recent progresses on metal halide perovskite-based material as potential photocatalyst. Catalysts, 2020, 10(6): 709
134. Li J M, Cao H L, Jiao W B, et al. Biological impact of lead from halide perovskites reveals the risk of introducing a safe threshold. Nature Communications, 2020, 11(1): 310
135. Chu L, Ahmad W, Liu W, et al. Lead-free halide double perovskite materials: A new superstar towards green and stable optoelectronic applications. Nano-Micro Letters, 2019, 11(1): 16
136. Xie B K, Chen D Y, Li N J, et al. Lead-free $Cs_3Bi_2Br_9$ perovskite *in-situ* growth on 3D flower-like g-C_3N_4 microspheres to improve photocatalytic performance. Chemical Engineering Journal, 2023, 452: 139662
137. Chakraborty S, Xie W, Mathews N, et al. Rational design: A high-throughput computational screening and experimental validation methodology for lead-free and emergent hybrid perovskites. ACS Energy Letters, 2017, 2(4): 837–845
138. Kamat P V, Bisquert J, Buriak J. Lead-free perovskite solar cells. ACS Energy Letters, 2017, 2(4): 904–905
139. Feng Y M, Chen D M, Zhong Y, et al. A lead-free 0D/2D $Cs_3Bi_2Br_9/Bi_2WO_6$ S-scheme heterojunction for efficient photoreduction of CO_2. ACS Applied Materials & Interfaces, 2023, 15(7): 9221–9230
140. Li N Y, Chen X J, Wang J, et al. ZnSe nanorods–$CsSnCl_3$ perovskite heterojunction composite for photocatalytic CO_2 reduction. ACS Nano, 2022, 16(2): 3332–3340
141. Wang X D, Huang Y H, Liao J F, et al. *In situ* construction of a Cs_2SnI_6 perovskite nanocrystal/SnS_2 nanosheet heterojunction with boosted interfacial charge transfer. Journal of the American Chemical Society, 2019, 141(34): 13434–13441
142. Zhang Z Z, Yang Y Y, Wang Y Y, et al. Revealing the A-site effect of lead-free $A_3Sb_2Br_9$ perovskite in photocatalytic C(sp^3)–H bond activation. Angewandte Chemie International Edition, 2020, 59(41): 18136–18139
143. Sheng J, He Y, Huang M, et al. Frustrated Lewis pair sites boosting CO_2 photoreduction on Cs_2CuBr_4 perovskite quantum dots. ACS Catalysis, 2022, 12(5): 2915–2926